Response surface methodology based on central composite design for simultaneous adsorption of rare earth elements using nanoporous calcium alginate/carboxymethyl chitosan microbiocomposite powder containing Ni0.2Zn0.2Fe2.6O4 magnetic nanoparticles: Batch and column studies

Hamedreza Javadian, Montserrat Ruiz, Ana Maria Sastre

PII: S0141-8130(19)39572-8

DOI: https://doi.org/10.1016/j.ijbiomac.2020.03.131

Reference: BIOMAC 15082

To appear in: *International Journal of Biological Macromolecules*

Received date: 22 November 2019

Revised date: 20 February 2020

Accepted date: 14 March 2020

Please cite this article as: H. Javadian, M. Ruiz and A.M. Sastre, Response surface methodology based on central composite design for simultaneous adsorption of rare earth elements using nanoporous calcium alginate/carboxymethyl chitosan microbiocomposite powder containing Ni0.2Zn0.2Fe2.6O4 magnetic nanoparticles: Batch and column studies, *International Journal of Biological Macromolecules* (2020), https://doi.org/10.1016/j.ijbiomac.2020.03.131

Response surface methodology based on central composite design for simultaneous adsorption of rare earth elements using nanoporous calcium alginate/carboxymethyl chitosan microbiocomposite powder containing $Ni_{0.2}Zn_{0.2}Fe_{2.6}O_4$ magnetic nanoparticles: Batch and column studies

Hamedreza Javadian[a,*], Montserrat Ruiz[b], Ana Maria Sastre[a]

[a]Department of Chemical Engineering, ETSEIB, Universitat Politècnica de Catalunya, Diagonal 647, 08028 Barcelona, Spain

[b]Department of Chemical Engineering, EPSEVG, Universitat Politècnica de Catalunya, Av. Víctor Balaguer, s/n, 08800 Vilanova i la Geltrú, Spain

[*]Corresponding author.

Email addresses: hamedreza.javadian@yahoo.com; hamedreza.javadian@upc.edu

Abstract

In this research paper, the utilization of the magnetic calcium alginate/carboxymethyl chitosan/$Ni_{0.2}Zn_{0.2}Fe_{2.6}O_4$ (CA/CMC/$Ni_{0.2}Zn_{0.2}Fe_{2.6}O_4$) was investigated for the simultaneous aqueous adsorption of Nd (III), Tb (III), and Dy (III). The magnetic products were characterized by FE-SEM, EDX, XRD, FT-IR, TGA, and VSM techniques. The saturation magnetization value for $Ni_{0.2}Zn_{0.2}Fe_{2.6}O_4$ and CA/CMC/$Ni_{0.2}Zn_{0.2}Fe_{2.6}O_4$ was found to be 45.87 and 14.14 emu/g, respectively. Using RSM, a quadratic polynomial equation was obtained to predict the adsorption efficiency of each ion. Under the conditions of pH = 5.5, adsorbent dosage of 0.1 g, initial concentration of 30 mg/L, and contact time of 53 min predicted by RSM, the adsorption efficiencies of Nd (III), Tb (III), and Dy (III) were respectively 95.72, 96.17, and 99.44 %. The isotherm and kinetic data were respectively fitted well with Freundlich and pseudo-second-order (PSO) models. The desorption of the loaded ions was effectively carried out by 0.2 M HNO_3, and the adsorbent was consecutively utilized with 2.54, 1.63, and 1.16 % decrease in adsorption efficiency for Nd (III), Tb (III), and Dy (III), respectively, after the forth cycle. Additionally, the adsorption behavior of the CA/CMC/$Ni_{0.2}Zn_{0.2}Fe_{2.6}O_4$ towards Nd (III), Tb (III), and Dy (III) was studied by using a fixed-bed column technique.

Keywords: Calcium alginate, Carboxymethyl chitosan, $Ni_{0.2}Zn_{0.2}Fe_{2.6}O_4$, Adsorption, Rare earth elements, RSM.

1. Introduction

Rare earth elements (REEs) are regularly alluded in terms of "seeds of technology" due to their utilization in electronic devices, high strength lasting magnets, green energy sectors, lasers, automotive catalytic converters, fiber superconductors/optics, etc [1,2]. Because of the progressing advancement in new trend-setting innovations, there is an over-expanding interest for REEs in the universal markets, with an accentuation on distinguishing new origins to guarantee satisfactory supply for utilizing in the present and future. This issue becomes more important since more than 90 % of mine production of rare earth occurs in China, and its REEs export was decreased 19015 tons from 2009 to 2012, leading to serious problems for REE users outside of China. Therefore, REEs recovery from wastes has been one of the most incredible worries in the ongoing years [3].

A few techniques, such as solvent extraction, chemical precipitation, ion exchange, membrane separation, adsorption and so on, have been applied for the REEs recovery [4,5]. Investigators have noted adsorption as a standout technique because of being easy, cost-effective, and environmentally friendly for REEs recovery in comparison with the regular techniques [6].

Alginate, as a natural biopolymer, is extracted from brown algae. Some of its benefits, such as biodegradability, biocompatibility, being cheap and nontoxic, make it a great potential material to be broadly and effectively utilized in water treatment [7-10]. It tends to be utilized to produce hydrogels under conditions of moderate pH and temperatures. Alginate can likewise be altered via physicochemical procedures to enhance its chemical and mechanical strength [11]. In this manner, its adsorption behavior can be increased by raising its adsorption capacity [12]. The utilization of alginate in the form of hydrogel beads is a typical technique to enhance its adsorption capacity [13].

Chitosan-based adsorbent materials are broadly applied for the adsorption removal of contaminations aqueous solution [14]. Chitosan possesses valuable characteristics, for example, biodegradability, hydrophilicity, nontoxicity, biocompatibility, high mechanical strength, film preparation, and antibacterial characteristics [15]. Its chemical structure contains amino ($-NH_2$) and hydroxyl (-OH) groups as major active functional groups for adsorption of metal ions from aqueous media [16,17]. The dissolvability of chitosan can be enhanced by modifying its structure with -COOH groups without influencing on the mentioned characteristics [18]. Besides, the carboxyl gathering presented in carboxymethyl chitosan (CMC) is additionally useful for the adsorption of metal ions.

It is necessary to easily separate adsorbents that are applied in the form of ultrafine powder for the separation of metal ions from aqueous media. For this purpose, centrifugation and filtration methods are not efficient to completely separate such a powder from aqueous media, while adsorbents having magnetic properties can be easily separated using an external magnetic field [19]. The active surface and small size of nanoparticles lead to their easy aggregation in aqueous media [20]. To solve this issue, amending the stability, increasing the application of magnetic nanoparticles, and their combining with biopolymers such as alginate and carboxymethyl chitosan could be considered as effective methods.

The goal of this study was to synthesize the CA/CMC/$Ni_{0.2}Zn_{0.2}Fe_{2.6}O_4$ as a magnetic adsorbent for simultaneous adsorption of Nd (III), Tb (III), and Dy (III) ions from aqueous solution. The adsorbent was analyzed by FE-SEM, EDX, XRD, FT-IR, TGA, and VSM techniques. The influences of adsorbent dosage, contact time, and initial concentration as main parameters were studied, and RSM-CCD was used to optimize them. The kinetic and isotherm

models were applied for fitting the experimental data. The performance of the CA/CMC/$Ni_{0.2}Zn_{0.2}Fe_{2.6}O_4$ was also evaluated in a fixed-bed column.

2. Materials and methods

2.1. Materials and reagents

Carboxymethyl chitosan and sodium alginate were purchased from Nantong Chem-Base Co, China, and PanReac AppliChem, respectively. $Nd(NO_3)_3.6H_2O$, $Tb(NO_3)_3 \cdot 6H_2O$, $Dy(NO_3).5H_2O$, $Zn(NO_3)_2$, $Fe(NO_3)_3.6H_2O$, $Ni(NO_3)_2 \cdot 6H_2O$, $CaCl_2$, and glutaraldehyde were bought from Sigma-Aldrich. Analytical grade materials were used without further purification. The experiment solutions of Nd (III), Tb (III), and Dy (III) ions were made by dilution of 1000 mg/L of ions. HNO_3 or NaOH solution with the molarity of 0.1 was utilized to carefully adjust the pH of the solutions.

2.2. Instrumentation and characterization

The record of FT-IR spectra were performed from 4000 to 450 cm^{-1} on a PerkinElmer, USA, by the KBr disk method. To identify the crystalline structure of the product, XRD pattern was taken down on a GBC MMA instrument with CuK_α radiation (wavelength $\lambda = 0.154$ nm) in the 2θ range of 10-70°. The morphological structure and particle size of the products were determined by FE-SEM (Zeiss Neon-40, Germany). The magnetic characteristics of the products were studied using VSM (Daghigh Kavir Corporation, Iran) at room temperature (RT). Thermal analyses were done on a Mettler TGA/SDTA 851e/LF/1100 thermobalance. The temperature of the samples was increased from RT to 1000 $^\circ$C at rate = 10 $^\circ$C/min under a constant flow of N_2. For analyzing the concentration of Nd (III), Tb (III), and Dy (III), an Agilent 4100 MP-AES Spectrometer was used. The Design Expert software, version 10, was utilized to define the experimental design by CCD and analyze the regression of the experimental data.

2.3. Synthesis of the $Ni_{0.2}Zn_{0.2}Fe_{2.6}O_4$ magnetic nanoparticles

The $Ni_{0.2}Zn_{0.2}Fe_{2.6}O_4$ magnetic nanoparticles were synthesized using hydrothermal method. A mixture of 0.2 M Ni^{2+}, 0.2 M Zn^{2+} and 2.6 M Fe^{3+} was prepared in HCl solution, and then NaOH solution was added into mixed solution under nitrogen gas and the mixture pH value was adjusted to 10.5. 0.3 g of CTAB was added to the mixture, and then it was placed into an autoclave (Teflon-lined stainless steel) and maintained at 200 °C of an oven for 8 h for hydrothermal treatment. The temperature of the autoclave was naturally decreased to RT, and the precipitate was collected and rinsed several times with deionized water to reach neutral pH. Finally, the obtained particles were dried at 50 °C.

2.4. Synthesis of the CA/CMC/$Ni_{0.2}Zn_{0.2}Fe_{2.6}O_4$ magnetic bionanocomposite

The synthesis procedure of the CA/CMC/$Ni_{0.2}Zn_{0.2}Fe_{2.6}O_4$ was as follows: Sodium alginate (1 g) was dissolved in 80 mL of deionized water at RT using a laboratory stirrer. 0.5 g of the carboxymethyl chitosan powder was added into the solution and homogeneously mixed. 0.7 g of the $Ni_{0.2}Zn_{0.2}Fe_{2.6}O_4$ was added to the mixture of the biopolymers. To obtain a homogeneous blend solution, the mixture of biopolymers and magnetic particles was stirred at RT for 24 h. Then, it was added to the solution of calcium chloride 0.05 M and 2 % glutaraldehyde for the gelation process. An external magnetic field was used to separate the resulting bionanocomposite from solution, and then it was washed several times with deionized water for removing remaining calcium chloride and glutaraldehyde until the pH value the solution was reached 7. The CA/CMC/$Ni_{0.2}Zn_{0.2}Fe_{2.6}O_4$ bionanocomposite was dried at 50 °C. Finally, it was powdered.

2.5. Batch adsorption

The adsorption experiments of Nd (III), Tb (III), and Dy (III) by the CA/CMC/$Ni_{0.2}Zn_{0.2}Fe_{2.6}O_4$ bionanocomposite were done in 125 mL flasks containing 50 mL solutions prepared from the

dilution of 1000 mg/L stock solutions at different pHs, adsorbent dosages, contact times, and initial concentrations with the ratio of 1:1:1. The agitation of the flasks was carried out on a laboratory shaker (rpm = 180). After adsorption process for a predefined time, the adsorbent was externally separated by a magnetic field, and the adsorption efficiency and adsorption capacity of the metal ions by the CA/CMC/$Ni_{0.2}Zn_{0.2}Fe_{2.6}O_4$ were computed using the equations as following:

$$\text{Adsorption efficiency (\%)} = (C_0 - C_e)/C_o \times 100 \quad (1)$$

$$q_e = (C_0 - C_e) \times V/m \quad (2)$$

$$q_t = (C_0 - C_t) \times V/m \quad (3)$$

Where q_e and q_t (mg/g) respectively refer to the quantities of metal ion adsorbed on the adsorbent at equilibrium and adsorption time t (min), C_0 (mg/L) is the initial concentration of metal ion, and C_e (mg/L) is the equilibrium concentration of metal ion. Moreover, C_t refers to the concentration of metal ion in solution at time t, V is the volume (L) of solution, and m refers to the weight (g) of the adsorbent.

2.6. Central composite design

Experimental design is applied by investigators to decrease the number of experiments in the adsorption process. It also presents helpful information about the effect of independent parameters individually and/or interactively that leads to a decrease in experimental error [21]. RSM was utilized to model the adsorption process of the ions by investigating the independent variables including adsorbent dosage, contact time, initial concentration, and response (ions adsorption efficiency). For simultaneous adsorption of Nd (III), Tb (III), and Dy (III) ions by the CA/CMC/$Ni_{0.2}Zn_{0.2}Fe_{2.6}O_4$ by using batch mode, CCD was utilized at five levels (-α (-2), low (-1), central (0), high (+1) and +α (+2)) (**Table 1**).

Analysis of variance (ANOVA) was used to obtain information about the adequacy of the models by evaluating coefficient of determination (R^2), lack of fit, and the Fisher test (F-value) values [22]. The quadratic polynomial model for response versus the independent variables was presented as follows [23]:

$$Y = \beta_0 + \sum_{i=1}^{k} \beta_i x_i + \sum_{i=1}^{k} \sum_{j=1}^{k} \beta_{ij} x_i x_j + \sum_{i=1}^{k} \beta_{ii} x_i^2 + \varepsilon \quad (4)$$

Where Y refers to the predicted response (adsorption efficiency), and β_0, β_i, β_{ii}, and β_{ij} respectively refer to the constant coefficient, linear coefficient, quadratic coefficient, and interaction coefficient. Notably, x_i and x_j are the independent variables, k shows the number of the independent variables, and ε is the residual error.

2.7. Column mode

Fixed-bed column investigation is necessary to successfully design a process and study the behavior of adsorbent in a large-scale utilization. To investigate the fixed-bed column, a column made of glass with an internal diameter of 0.5 cm and a length of 12 cm was used. 0.3 g of the adsorbent was mixed with 1.8 g of acid-cleaned sand, and the mixture was packed in the column between two layers of glass wool. Sand was applied to decrease the pressure drop. The final height of the mixture in the column was about 6.5 cm. An upward flow rate (1 mL/min) was provided by a peristaltic pump to flush the column with deionized water for 1 h. Then, the column was fed with a ternary solution of the ions at 30 mg/L initial concentration as an influent for 520 min. The collection of the effluent was performed every 10 min by a fraction collector, and the concentration of the ions was determined by Agilent 4100 MP-AES Spectrometer.

The breakthrough curve is usually shown by C_t/C_0 versus time. The amount of ion adsorbed (q_{total}, mg) was obtained by calculating the curve of breakthrough (upper area) by using the following equation:

$$q_{total} = \frac{Q}{1000}\int_{t_0}^{t_{total}}(1 - \frac{C_t}{C_0}) \quad (5)$$

Where Q is the flow rate (mL/min) that was determined via division of the effluent volume (V_{eff}, mL) to the total time (t_{total}, min):

$$Q = \frac{V_{eff}}{t_{total}} \quad (6)$$

The entire quantity of the metals passed through the column (mg) was obtained by the following equation:

$$m_{total} = \frac{C_0 \times Q \times t_{total}}{1000} \quad (7)$$

The total metal adsorption efficiency was calculated from the ratio of the entire quantity of the metals sent to the column (q_{total}) to the metal mass adsorbed (m_{total}) by the following equation:

$$Adsorption\ efficiency = \frac{q_{total}}{m_{total}} \times 100 \quad (8)$$

The capacity of equilibrium adsorption (q_e (mg/g)) and the equilibrium metal concentration (C_e (mg/L)) were respectively computed using Eqs. (9) and (10) as following:

$$q_e = \frac{q_{total}}{m} \quad (9)$$

$$C_e = \frac{m_{total} - q_{total}}{V_{eff}} \times 100 \quad (10)$$

Where m shows the adsorbent mass (g).

2.8. Error analysis

Error analysis was used to optimize the fitness of the experimental data obtained from the non-linear approach. In this study, Chi-square (χ^2) was employed to compare the validity of each model by the following equation:

$$\chi^2 = \sum_{i=1}^{n} \frac{(q_{e,exp} - q_{e,cal})^2}{q_{e,cal}} \quad (11)$$

Where n shows the number of data points, $q_{e,exp}$ is the experimental capacity of the adsorbent, and $q_{e,cal}$ refers to the computed capacity of the adsorbent.

3. Results and discussion

3.1. Products characterization

Fig. 1 indicates the XRD pattern of the $Ni_{0.2}Zn_{0.2}Fe_{2.6}O_4$. The peaks at 2θ = 18.13°, 30.07°, 35.50°, 37.08°, 43.07°, 53.95°, 56.96° and 63.89° are in agreement with the standard pattern of nickel zinc ferrite (JCPDS 08-0234) [24]. Full Width at Half Maximum (FWHM) of the strongest reflection of the XRD pattern was used to estimate the average crystal size based on the Scherrer equation as following [25]:

$$D = k\lambda/\beta \cos\theta \quad (12)$$

Where k refers to the function of shape (k = 0.89), and λ refers to the radiation X-ray wavelength. Moreover, β and θ respectively refer to the Full Width at Half Maximum (FWHM) at 2θ = 35.50°, and the diffraction angle. Based on the Scherrer equation, the calculated value of D was 27.68 nm.

The FE-SEM image of the $Ni_{0.2}Zn_{0.2}Fe_{2.6}O_4$ in **Fig. 2A** indicates that the synthesized particles are nearly spherical in shape and homogenous in distribution with a diameter less than 100 nm. **Fig. 2B** shows the distribution of the magnetic nanoparticles on the surface of the

CA/CMC or embedding with the CA/CMC that confirms the successful synthesis of the CA/CMC/$Ni_{0.2}Zn_{0.2}Fe_{2.6}O_4$ magnetic bionanocomposite.

Fig. 3 indicates the FT-IR spectrum for CA, CMC, $Ni_{0.2}Zn_{0.2}Fe_{2.6}O_4$ and CA/CMC/$Ni_{0.2}Zn_{0.2}Fe_{2.6}O_4$. The FT-IR spectrum for CA and CMC in **Figs. 3A** and **3B**, respectively, shows O-H stretching vibration at 3389 (CA) and 3436 (CMC) cm^{-1}, carboxyl groups asymmetrical stretching at 1622 (CA) and 1631 (CMC) cm^{-1}, carboxyl groups symmetrical stretching at 1423 (CA) and 1411 (CMC) cm^{-1} and C-O-C stretching at 1052 (CA) and 1061 (CMC) cm^{-1} [26,27]. The FT-IR spectrum of the $Ni_{0.2}Zn_{0.2}Fe_{2.6}O_4$ in **Fig. 3C** shows a broad band at around 3424 cm^{-1} and less intensive band at 1633 cm^{-1} that are related to the O-H groups stretching vibration [28]. The bands at 2925 and 2853 cm^{-1} are assigned to the anti-symmetric and symmetric C-H vibrations of CTAB [29]. The band at 567 cm^{-1} attributes to intrinsic metal stretching vibrations at the tetrahedral site (Fe-O), and octahedral metal stretching (M-O) is seen at around 478 cm^{-1} [28]. The successful synthesis of the CA/CMC/$Ni_{0.2}Zn_{0.2}Fe_{2.6}O_4$ can be confirmed by comparing its spectrum shown in **Fig. 3D** with other spectra.

N_2 adsorption–desorption isotherm and the corresponding Barrett-Joyner-Halenda (BJH) pore size distribution of the CA/CMC/$Ni_{0.2}Zn_{0.2}Fe_{2.6}O_4$ are shown in **Fig. 4**. The nitrogen adsorption-desorption isotherm for the sample in **Fig. 4A** is assigned to type IV indicating the presence of mesoporous structure. The Brunauer–Emmett–Teller (BET) surface area, pore volume, and pore size (obtained by the BJH method (**Fig. 4B**)) were calculated to be 7.1143 m^2/g, 0.034971 cm^3/g, and 19.0379 nm, respectively. The results clearly demonstrate the formation of CA/CMC/$Ni_{0.2}Zn_{0.2}Fe_{2.6}O_4$ with nano size pores.

EDX was recorded to analyze the elements of the products, and the results are presented in **Fig. 5**. **Fig. 5A** shows Ni, Zn, Fe, and O peaks that confirm the formation of the $Ni_{0.2}Zn_{0.2}Fe_{2.6}O_4$. The elemental analysis of the nanocomposite in **Fig. 5B** represents similar peaks available in **Fig. 5A** along with the new peaks for N and Ca because of combining the nanoparticles with CA and CMC. Sodium peak is not seen in the spectrum of the CA/CMC/$Ni_{0.2}Zn_{0.2}Fe_{2.6}O_4$, suggesting that sodium ions were released completely from the matrix of sodium alginate into the solution during the crosslinking reaction process of sodium alginate with calcium. EDX spectrum was also recorded after the adsorption process and the result is presented in **Fig. 5C**. The existence of Nd (III), Tb (III), and Dy (III) in the spectrum strongly confirms the successful adsorption of these ions by the CA/CMC/$Ni_{0.2}Zn_{0.2}Fe_{2.6}O_4$.

The CA/CMC/$Ni_{0.2}Zn_{0.2}Fe_{2.6}O_4$ weight loss curve recorded in the range of RT to 1000 $^{\circ}$C is demonstrated in **Fig. 6**. As it is seen, there are three different weight-loss steps in the TGA curve of the CA/CMC/$Ni_{0.2}Zn_{0.2}Fe_{2.6}O_4$. Obviously, the first step (around 190 $^{\circ}$C) with a weight loss of 8.77 % can be attributed to trapped and physisorbed water evaporation. The second step between around 190 and 550 $^{\circ}$C is the largest weight loss with the amount of 35.08 % that could be due to sorption and degradation of CA and CMC. The last step with 22.95 % weight loss at temperature beyond 550 $^{\circ}$C could be related to the further decomposition of CA and CMC and their conversion to CO_2 and H_2O. At the end of the process, the residue percentage is about 33.2 % that is principally assigned to the presence of the $Ni_{0.2}Zn_{0.2}Fe_{2.6}O_4$.

According to the magnetic hysteresis loops in **Fig. 7A**, the magnetic saturation value for $Ni_{0.2}Zn_{0.2}Fe_{2.6}O_4$ is about 45.87 emu/g that indicates the superparamagnetic behavior of the synthesized product. Based on **Fig. 7B**, it is obvious that the process of the synthesis of the CA/CMC/$Ni_{0.2}Zn_{0.2}Fe_{2.6}O_4$ results in a decrease of saturation magnetization to the value of 14.14

emu/g. This decline is due to combining the magnetic nanoparticles by CA and CMC. Despite this difference, the CA/CMC/$Ni_{0.2}Zn_{0.2}Fe_{2.6}O_4$ can be easily separated from aqueous solution using an external magnetic field to avoid secondary pollution. **Fig. 7C** shows the easy separation of the metal ions-loaded adsorbent from the solution by applying an external magnetic field.

3.2. Effect of pH

Solution pH is considered as an essential parameter in the process of adsorption owing to its effect on metal ions solubility, counter ions concentration on the adsorbent functional groups, and the adsorbate ionization degree. In this study, the influence of pH value on the process of adsorption was considered from 1.5 to 5.5. The pH_{ZPC} of the CA/CMC/$Ni_{0.2}Zn_{0.2}Fe_{2.6}O_4$ was found to be 6. Since the precipitation of the ions may occur at pH values higher than 5.5, the experiments were carried out near to pH_{ZPC}; therefore, adsorption of the ions were not studied at pH > 5.5. As it is indicated in **Fig. 8**, the adsorption efficiency for the ions at pH = 1.5 is zero that indicates a highly acidic solution strongly affects the ions adsorption. At acidic solution, H^+ concentration and its mobility are high that lead to strong competition with the ions to occupy the active sites. Actually, the protonation of the active sites occurs in a low value of pH, leading to electrostatic repulsion between positively charged cations and positively charged active sites; therefore, the value of adsorption efficiency is low. As the pH of solution increases, the amount of H^+ being available in the solution decreases; hence, more negatively charged sites are available that facilitate higher uptake of the ions by electrostatic attraction [30]. According to the obtained results, further adsorption studies were performed at pH = 5.5 as an optimum value.

3.3. Central composite design

A total number of 32 experiments suggested by Design Expert 10.0 was performed to investigate the interaction of contact time (X_1), adsorbent dosage (X_2), Nd (III) concentration (X_3), Tb (III)

concentration (X_4), and Dy (III) concentration (X_5). **Table 1** indicates the design of experiments plus the predicted and actual values (adsorption efficiency (%)). Quadratic regression modeling was applied between the response and independent variables for each metal, and the obtained equations were as follows:

Nd (III) adsorption efficiency (%)= 45.421 + 1.866 X_1 + 514.024 X_2 – 0.571 X_3 – 1.322 X_4 + 0.175 X_5 – 0.0043 X_1X_3 + 0.00312 X_1X_4 – 0.00255 X_1X_5 – 2.27 X_2X_1 + 1.796 X_2X_3 + 1.351 X_2X_4 + 0.759 X_2X_5 + 0.00712 X_3X_4 -0.00258 X_3X_5 + 0.00469 X_4X_5 – 0.0126 $X1^2$ – 1237.07 X_2^2 – 0.000393 X_3^2 + 0.00122 X_4^2 – 0.00378 X_5^2

(13)

Tb (III) adsorption efficiency (%) = 51.793 + 1.663 X_1 + 410.645 X_2 – 0.502 X_3 – 0.603 X_4 + 0.24 X_5 – 7.549 X_1X_3 + 1.073 X_1X_4 – 1.132 X_1X_5 – 2.253 X_2X_1 + 1.651 X_2X_3 + 1.185 X_2X_4 + 1.283 X_2X_5 + 0.00328 X_3X_4 – 0.00178 X_3 X_5 + 0.00243 X_4X_5 -0.0124 $X1^2$ -1059.01 X_2^2 – 0.0001808 X_3^2 + 0.000553 X_4^2 – 0.00103X_5^2

(14)

Dy (III) adsorption efficiency (%) = 58.691 + 1.632 X_1 + 405.813 X_2 - 0.354 X_3 – 0.778 X_4 – 0.315 X_5 – 0.00156 X_1X_3 + 0.00241X_1X_4 – 0.000818 X_1X_5 – 2.405 X_2X_1 + 1.486 X_2X_3 + 1.371 X_2X_4 + 1.272 X_2X_5 + 0.00183 X_3X_4 – 0.00243 X_3X_5 + 0.00253 X_4X_5 – 0.0122 $X1^2$ – 1039.17 X_2^2 + 0.000237 X_3^2 + 0.000437 X_4^2 – 0.0000959 X_5^2

(15)

The reliability of the models was examined by ANOVA. ANOVA represents the significance of variations associated with the models in comparison with the variations related to the experimental data [22]. The values of R^2 and R_{adj}^2 in **Table 2** indicate a good agreement between the predicted and experimental data. In **Table 2**, the F-values with a very low probability value

of 0.0001 show that the predicted models are statistically significant. The ‘Adequate precision’’ value for Nd (III), Tb (III), and Dy (III) obtained by ANOVA are favorable as a value > 4 is preferable [31]. Additionally, the coefficient of variation value (C.V. %) is low, showing the reliability of the modeling. As can be observed from **Fig. 9**, the dispersal of the data points is not evident. A relatively straight line of normal probability plot should follow a nearly straight line to be favorable. In addition, the residuals are dispersed randomly in **Figs. 10** and **11**, indicating a favorable fitness between the predicted and experimental data.

3.4. Three-dimensional response surface plot

To understand the main and interaction influences of two parameters in the adsorption process, 3D response surface plots are applied by considering them as function of adsorption efficiency while other factors are kept at constant values. The interactive effects of contact time, adsorbent dosage, and initial concentration of the ions are presented in **Figs. 12A-I**.

The effect of contact time and adsorbent dosage simultaneously on the ions adsorption is seen in **Figs. 12A-C**. It is evident that adsorption efficiency increases by enhancing contact time and adsorbent dosage. An increase in adsorption efficiency by an enhancement in the dosage of the adsorbent can be interpreted that increasing adsorbent dosage supplies more surface area and active binding sites for the ions adsorption onto the adsorbent [32]. According to the results of affecting time on the adsorption efficiency, two phases for the adsorption of the metal ions are seen as follows: the first phase that is sharper is related to the large number of the active sites that are empty on the adsorbent surface and high metal ions concentration. The second phase is assigned to the gradual decrease in the active sites, the decrease in intra-particle diffusion with the contact time, and the decrease in driving force that lead to an equilibrium state.

The concurrent influence of contact time and initial concentration in **Figs. 12D-F** shows higher adsorption efficiency of the ions at lower initial concentration since the adsorbent surface

area is larger for the adsorption of the metal ions. An enhancement in the concentration of ions causes a decrease in adsorption efficiency because of decreasing available active sites for the ions adsorption as a result of the adsorption sites saturation [33]. Due to the higher ratio of initial number of the ions to the available adsorption sites at a higher ions concentration, lower adsorption efficiency is expected. It can be seen that increasing contact time beyond the optimum value leads to a decrease in adsorption efficiency for all the ions that could be due to the release or desorption of some ions from the substrate surfaces [34].

Figs. 12G-I are related to the simultaneous influence of adsorbent dosage and initial concentration. An increase in adsorbent dosage causes that adsorption efficiency increases due to the reason mentioned above. However, increasing adsorbent dosage at more than the optimum value leads to a decrease in adsorption efficiency due to the agglomeration of the adsorbent particles and screening effect. The total surface area of the adsorbent declines by such agglomeration, resulting in a reduction in the ions adsorption efficiency [35].

3.5. Confirmation experiments

The validity of the RSM model was investigated by performing four experiments for Nd (III), Tb (III), and Dy (III) ions adsorption onto the adsorbent. The adsorption efficiency acquired for each ion under the conditions given by CCD was compared with the value predicted by RSM. As can be observed from the obtained results presented in **Table 3**, difference between the values obtained from the experiments and predicted by the model results in error percentage in the range of 0.54-1.87, 0.58-2.28, and 0.61-2.11 % for Nd (III), Tb (III), and Dy (III), respectively. At pH = 5.5, the adsorption efficiency under the conditions given by the model (adsorbent dosage = 0.1 g, contact time = 53 min, and initial concentration = 30 mg/L) was calculated to be 95.72, 96.17, and 99.44 % with 1.17, 0.58, and 0.61 % error for Nd (III), Tb (III), and Dy (III),

respectively, indicating its agreement with the experimental value. The errors show the capability of the RSM model for the prediction of values that are favorably in accordance with the experimental data.

3.6. Batch adsorption kinetic studies

Kinetic investigations were carried out using the solutions with the volume 50 mL prepared at 30 mg/L of Nd (III), Tb (III), and Dy (III) ions that were contacted with 0.09 g of the adsorbent at various times. Non-linear pseudo-first-order (PFO), PSO, and intra-particle diffusion (IPD) models were applied to model the kinetic data of Nd (III), Tb (III), and Dy (III) ions adsorption. The equations are as follows [36,37]:

$q_t = q_e\,(1 - \exp^{-K_1 t})$ PFO (16)

$q_t = K_2 q_e^2 t/1 + K_2 q_e t$ PSO (17)

$q_t = K_i t^{0.5} + C$ IPD (18)

Where K_1 (1/min), K_2 (g/mg min), and K_i (1/min) respectively refer to the PFO rate constant, PSO rate constant, and the rate constant of IPD. Moreover, C provides information about the thickness of the boundary layer: higher value of C is related to the boundary layer diffusion influence.

The initial rate of adsorption (h) can be computed using K_2 and q_e values by the following equation:

$h = K_2 q_e^2$ (19)

The values of kinetic parameters are shown in **Table 4**. As it is obvious from the results, the highest values of R^2 and the lowest values of $\square^2$ obtained by PSO shows that the main mechanism for controlling the adsorption of Nd (III), Tb (III), and Dy (III) ions onto the CA/CMC/$Ni_{0.2}Zn_{0.2}Fe_{2.6}O_4$ is chemisorption. The values of R^2 obtained by IPD model show that

the adsorption of the ions is a multi-stage process. The stages were related to the strong electrostatic forces of attractions between the ions and the functional groups of the adsorbent, and gradual adsorption by the ions diffusion into the pores of the adsorbent until the occupation of most or all of the active sites. In addition, IPD model was not the sole rate-limiting step (the related plots do not pass through the origin).

3.7. Batch adsorption isotherm studies

Batch isotherm experiments were performed using 50 mL of metal ions solutions at different concentrations in the range of 30-180 mg/L contacting with 0.09 g of the CA/CMC/$Ni_{0.2}Zn_{0.2}Fe_{2.6}O_4$ at pH = 5.5. The data obtained at equilibrium were modeled by Langmuir and Freundlich models that are respectively related to monolayer and multilayer adsorption. The nonlinear Langmuir and Freundlich models were used according to following equations [38,39]:

$$q_e = \frac{b\ q_m\ C_e}{(1+bC_e)} \quad \text{Langmuir} \quad (20)$$

$$q_e = K\ C_e^{1/n} \quad \text{Freundlich} \quad (21)$$

Where q_e and q_m (mg/g) respectively refer to the equilibrium adsorption and maximum adsorption capacities, and C_e (mg/L) shows the adsorbate equilibrium concentration. Moreover, b (L/mg) and K ($mg^{1-1/n}\ L^{1/n}/g$) respectively refer to Langmuir and Freundlich constants, and n shows adsorption intensity. Adsorption is favorable if $n > 1$.

The coefficient of determination (R^2) values and the corresponding parameters obtained by the models are presented in **Table 5.** The n values are 9, 9.26, and 9.71 for Nd (III), Tb (III), and Dy (III), respectively, showing a strong interaction between the CA/CMC/$Ni_{0.2}Zn_{0.2}Fe_{2.6}O_4$ and the metal ions. According to the values of R^2 and $\square^2$, it is obvious that Freundlich model better fits the experimental data than Langmuir model for Nd (III), Tb (III), and Dy (III) ions

adsorption. Consequently, the adsorption of the ions is multilayer adsorption, and the adsorption takes place on a non-uniform surface.

3.8. Ionic strength effect

The ions adsorption can be affected by the co-ions that are available in the solution. The influence of salt concentration, known as ionic strength, on the adsorption efficiency of the ions by the CA/CMC/$Ni_{0.2}Zn_{0.2}Fe_{2.6}O_4$ was evaluated using $NaNO_3$ at various concentrations ranging from 0.02 to 0.1 M, and the results are presented in **Fig. 13A**. As it is illustrated in **Fig. 13A**, the presence of $NaNO_3$ has a greater negative effect on the adsorption efficiency of Nd (III) in comparison with Tb (III) and Dy (III). The adsorption efficiency for Nd (III), Tb (III), and Dy (III) respectively decreases from 92.33 to 77.12, 93.91 to 85.6, and 96.25 to 91.43 % by an increase in $NaNO_3$ concentration. This phenomenon can be related to the competition between the metal ions and sodium ions for the available active adsorption sites of the adsorbent [40]. In addition, the aggregation of adsorbent could be heightened by enhancing ionic strength that results in a decrease in adsorption sites of adsorbent [41].

3.9. Thermodynamic parameters

Thermodynamic parameters are considered as key factors to realize the optimal condition and give further information regarding changes in inherent energetic related to adsorption process. The adsorption process was conducted at various temperatures (25, 35, and 45 $^{\circ}$C) to obtain ΔS° and ΔH° values based on the following equation:

$$\text{Ln } K_d = \frac{\Delta S^{\circ}}{R} - \frac{\Delta H^{\circ}}{RT} \quad (22)$$

Where R, T, and K_d respectively refer to the gas constant (8.314 J/mol K), temperature (K), and distribution coefficient that was obtained by the equation as following:

$$K_d = \frac{q_e}{C_e} \quad (23)$$

Where C_e refer to the equilibrium concentration in the solution (mg/L). ΔH° value for each metal is calculated from the slope of Ln K_d versus 1/T plot, and ΔS° value is computed from its intercept (**Fig. 13B**). The ΔG° values were also calculated at different temperatures by using the following equation:

$$\Delta G^\circ = - RT \text{ Ln } K_d \quad (24)$$

Table 6 shows the values of thermodynamic parameters. The ΔG° values for the ions are positive at all temperatures that show the process is non-spontaneous, and the adsorption of the ions onto the adsorbent requires additional energy from an external source. The lower values of ΔG° at higher temperatures mean that an increase in temperature leads to an increase in the tendency of spontaneous reaction. The ΔH° value > zero shows the endothermic adsorption of the metal ions, and the ΔS° value > zero expresses the increase in randomness at the interface of solid–solution during the metal ions fixation on the CA/CMC/$Ni_{0.2}Zn_{0.2}Fe_{2.6}O_4$ surface [39].

3.10. Reusability studies

The synthesized CA/CMC/$Ni_{0.2}Zn_{0.2}Fe_{2.6}O_4$ was utilized in four consecutive adsorption-desorption cycles to investigate its reusability. For this purpose, the adsorption of the ions by the CA/CMC/$Ni_{0.2}Zn_{0.2}Fe_{2.6}O_4$ was performed at initial concentration = 30 mg/L and pH = 5.5 with 0.1 g of the adsorbent for 53 min. The batch flask containing the CA/CMC/$Ni_{0.2}Zn_{0.2}Fe_{2.6}O_4$ and 50 mL of 0.2 M HNO_3 as eluent was shaken for 2 h for desorption of the ions loaded onto the adsorbents. Then, the adsorbent was separated by an external magnetic field from the HNO_3 solution, and the functional groups were neutralized by NaOH solution. The neutralized CA/CMC/$Ni_{0.2}Zn_{0.2}Fe_{2.6}O_4$ was then used for the adsorption of 30 mg/L of the ions in the next cycle.

The results of adsorption efficiency in four cycles are shown in **Fig. 13C**. Due to the decrease in the release of the ions and number of active sites by acid treatment during the cycles, the adsorption efficiency for Nd (III), Tb (III), and Dy (III) respectively decreases from 94.18 to 91.64, 96.45 to 94.82, and 98.33 to 97.17 %. After the last cycle, the adsorption efficiency of the CA/CMC/$Ni_{0.2}Zn_{0.2}Fe_{2.6}O_4$ indicates 2.54, 1.63, and 1.16 % lose for Nd (III), Tb (III), and Dy, respectively, in comparison with the first cycle. The results also indicated that the CA/CMC/$Ni_{0.2}Zn_{0.2}Fe_{2.6}O_4$ remained magnetic during the process of adsorption-desorption. According to the results, the adsorbent suitability for a practical application can be concluded.

3.11. Column mode

Fig. 14A presents the Nd (III), Tb (III), and Dy (III) ions adsorption breakthrough curves obtained from the fixed-bed column packed with the CA/CMC/$Ni_{0.2}Zn_{0.2}Fe_{2.6}O_4$. According to the obtained results, the breakthrough and exhaustion times that respectively correspond to C_e/C_0=0.05 and 0.95 are about 95 and 410 min for Nd (III), 105 and 430 min for Tb (III), and 120 and 440 min for Dy (III). Exhaust volume (V_{eff}) for Nd (III), Tb (III), and Dy (III) is respectively 410, 430, and 440 mL.

Nonlinear Thomas and Yan models were utilized to fit the experimental data of the fixed-bed column by Eq. (25) and Eq. (26), respectively.

$$\frac{C_t}{C_0} = \frac{1}{1+\exp\left(\frac{K_{Th}q_e x}{Q} - K_{Th}C_0 t\right)} \quad (25)$$

$$\frac{C_t}{C_0} = 1 - \frac{1}{1+(\frac{C_0 Q t}{q_e x})^a} \quad (26)$$

Where K_{Th} shows the rate constant (mL/min mg), a is a constant coefficient and q_e is the maximum adsorption capacity (mg/g), x is the mass of adsorbent (g), C_0 is the initial

concentration (mg/L) of the ions, C_t is outlet ions concentration (mg/L), t is the contact time (min), and Q is the flow rate (mL/min). K_{Th} , a, and q_e values are computed using the slope and intercept of the plot of $\frac{C_t}{C_0}$ against t.

The parameters obtained by the models (**Figs. 14B-D**) are indicated in **Table 7**. The adsorption capacity (q_e) for Nd (III), Tb (III), and Dy (III), calculated by Eq. (9), is respectively 22.70, 24.00, and 25.54 mg/g under the studied conditions. According to the values of R^2, both models can fit the experimental data well but Yan model presents higher values of R^2 in comparison with Thomas model. The rate constant value of Thomas (K_{Th}) for Nd (III) is higher than those of Tb (III), and Dy (III), showing higher intensity of Nd (III) adsorption onto the CA/CMC/$Ni_{0.2}Zn_{0.2}Fe_{2.6}O_4$, while the amount of maximum adsorption capacity (q_e) for Dy (III) is greater than the value obtained for Nd (III) and Tb (III). This is in conformity with the results achieved from experiments of batch adsorption.

4. Conclusion

In this paper, the CA/CMC/$Ni_{0.2}Zn_{0.2}Fe_{2.6}O_4$ was synthesized successfully by the gelation process of CA/CMC in the presence of the $Ni_{0.2}Zn_{0.2}Fe_{2.6}O_4$. RSM-CCD was applied to explore the influences of experimental parameters on Nd (III), Tb (III), and Dy (III) ions adsorption. The conditions predicted by RSM for optimum adsorption of 30 mg/L of the ions were 0.1 g of the adsorbent and 53 min contact time at pH = 5.5. The experimental data were fitted by isotherm and kinetic models. PSO kinetic model fitted the data better compared with IPD and PFO models. The data of equilibrium were fitted well with Freundlich model. The values of ΔH° revealed the endothermic adsorption process of the metal ions. 0.2 M HNO_3 was used for regeneration of the ion-loaded adsorbent, and the adsorbent was repeatedly used in four cycles

with more than 91, 94, and 97 % adsorption efficiency for Nd (III), Tb (III), and Dy (III), respectively, after the fourth cycle. Besides, the ions were successfully adsorbed in a continuous process by applying a packed-bed column, and the data were found to be fitted well by Thomas and Yan models. The results showed that the CA/CMC/$Ni_{0.2}Zn_{0.2}Fe_{2.6}O_4$ can be applied as a potential adsorbent in both adsorption modes (batch and column) for Nd (III), Tb (III), and Dy (III) ions adsorption.

Acknowledgments

This work has been supported by the Spanish Ministry of Economy and Competitiveness (Ref. CTM2017-83581-R). Hamedreza Javadian acknowledges the financial support received (Ref. BES-2015-072506).

References

[1] G.A. Moldoveanu, V.G. Papangelakis, Recovery of rare earth elements adsorbed on clay minerals. I. Desorption mechanism, Hydrometallurgy 117–118 (2012) 71–78.

[2] J. Ponou, L.P. Wang, G. Dodbiba, K. Okaya, T. Fujita, K. Mitsuhashi, T. Atarashi, G. Satoh, M. Noda, Recovery of rare earth elements from aqueous solution obtained from Vietnamese clay minerals using dried and carbonized parachlorella, J. Environ. Chem. Eng. 2 (2014) 1070-1081.

[3] W. Franus, M.M. Wiatros-Motyka, M. Wdowin, Coal fly ash as a resource for rare earth elements, Environ. Sci. Pollut. Res. 22 (12) (2015) 9464-9474.

[4] D. Sadovsky, A. Brenner, B. Astrachan, B. Asaf, R. Gonen, Biosorption potential of cerium ions using *Spirulina* biomass, J. Rare Earths 34 (2016) 644-652.

[5] F. Zhao, E. Repo, Y. Meng, X. Wang, D. Yin, M. Sillanpää, An EDTA-β-cyclodextrin material for the adsorption of rare earth elements and its application in preconcentration of rare earth elements in seawater, J. Colloid Interface Sci. 465 (2016) 215-224.

[6] K. Vijayaraghavan, R. Balasubramanian, Single and binary biosorption of cerium and europium onto crab shell particles, Chem. Eng. J. 163 (2010) 337-343.

[7] J.L. Wang, C. Chen, Biosorbents for heavy metals removal and their future, Biotechnol. Adv. 27(2) (2009) 195-226.

[8] H.A. Shawky, Improvement of water quality using alginate/montmorillonite composite beads, J. Appl. Polym. Sci. 119(4) (2010) 2371-2378.

[9] Y. Ma, P. Qi, J. Ju, Q. Wang, L. Hao, R. Wang, K. Sui, Y. Tan, Gelatin/alginate composite nanofiber membranes for effective and even adsorption of cationic dyes, Compos Part B Eng. 162 (2019) 671-677.

[10] F. Ahmadpoor, S.A. Shojaosadati, S.Z. Mousavi, Magnetic silica coated iron carbide/alginate beads: Synthesis and application for adsorption of Cu (II) from aqueous solutions, Int. J. Biol. Macromol. 128 (2019) 941-947.

[11] T. Guo, Y. Pei, K. Tang, X. He, J. Huang, F. Wang, Mechanical and drug release properties of alginate beads reinforced with cellulose, J. Appl. Polym. Sci. 134(8) (2016) 44495.

[12] Z.H. Hu, A.M. Omer, X.K. Ouyang, D. Yu, Fabrication of carboxylated cellulose nanocrystal/sodium alginate hydrogel beads for adsorption of Pb(II) from aqueous solution, Int. J. Biol. Macromol. 108 (2018) 149-157.

[13] R. Ahmad, A. Mirza, Adsorption of Pb (II) and Cu (II) by Alginate-Au-Mica bionanocomposite: Kinetic, isotherm and thermodynamic studies, Process Saf Environ. 109 (2017) 1-10.

[14] L. Zhang, Y. Zeng, Z. Cheng, Removal of heavy metal ions using chitosan and modified chitosan: A review, J. Mol. Liq. 214 (2016) 175-191.

[15] M. Li, J. Xu, R. Li, D. Wang, T. Li, M. Yuan, J. Wang, Simple preparation of aminothiourea-modified chitosan as corrosion inhibitor and heavy metal ion adsorbent, J Colloid Interface Sci. 417(3) (2014) 131-136.

[16] D.W. Cho, B.H. Jeon, C.M. Chon, Y. Kim, F.W. Schwartz, E.S. Lee, H. Song, A novel chitosan/clay/magnetite composite for adsorption of Cu(II) and As(V), Chem. Eng. J. 200-202(34) (2012) 654-662.

[17] L. Fan, C. Luo, Z. Lv, F. Lu, H. Qiu, Removal of Ag^{+} from water environment using a novel magnetic thiourea-chitosan imprinted Ag^{+}, J. Hazard. Mater. 194(11) (2011) 193-201.

[18] P.O. Boamah, Y. Huang, M. Hua, Q. Zhang, J. Wu, J. Onumah, L.K. Sam-Amoah, P.O. Boamah, Sorption of heavy metal ions onto carboxylate chitosan derivatives—A mini-review, Ecotoxicol. Environ. Saf. 116 (2015) 113-120.

[19] H. Yang, H. Li, J. Zhai, L. Sun, Y. Zhao, H. Yu, Magnetic prussian blue/graphene oxide nanocomposites caged in calcium alginate microbeads for elimination of cesium ions from water and soil, Chem. Eng. J. 246 (2014) 10-19.

[20] G. Reiss, A. Hütten, Magnetic nanoparticles: applications beyond data storage, Nat. Mater. 4 (2005) 725–726.

[21] D. Gusain, F. Bux, Y. Chandra Sharma, Abatement of chromium by adsorption on nanocrystalline zirconia using response surface methodology, J. Mol. Liq. 197 (2014) 131-141.

[22] Markandeya, N. Dhiman, S.P. Shukla, G.C. Kisku, Statistical optimization of process parameters for removal of dyes from wastewater on chitosan cenospheres nanocomposite using response surface methodology, J. Clean. Prod. 149 (2017) 597-606.

[23] V. Srivastava, Y.C. Sharma, M. Sillanpää, Application of response surface methodology for optimization of Co(II) removal from synthetic wastewater by adsorption on NiO nanoparticles, J. Mol. Liq. 211 (2015) 613–620.

[24] D. Ni, Z. Lin, P. Xiaoling, W. Xinqing, G. Hongliang, Preparation and characterization of nickel-zinc ferrites by a solvothermal method, Rare Metal Mat Eng. 44(9) (2015) 2126-2131.

[25] C. Tamez, R. Hernandez, J.G. Parsons, Removal of Cu (II) and Pb (II) from aqueous solution using engineered iron oxide nanoparticles, Microchem. J. 125 (2016) 97-104.

[26] R. Fabryanty, C. Valencia, F. Edi Soetaredjo, J. Nyoo Putro, S. Permatasari Santoso, A. Kurniawan, Y.H. Ju, S. Ismadji, Removal of crystal violet dye by adsorption using bentonite-alginate composite, J. Environ. Chem. Eng. 5 (2017) 5677-5687.

[27] S.P. Wu, X.Z. Dai, J.R. Kan, F.D. Shilong, M.Y. Zhu, Fabrication of carboxymethyl chitosan–hemicellulose resin for adsorptive removal of heavy metals from wastewater, Chin. Chem. Lett. 28 (2017) 625-632.

[28] A.S.A. Bakr, Y.M. Moustafa, E.A. Motawea, M.M. Yehia, M.M.H. Khalil, Removal of ferrous ions from their aqueous solutions onto $NiFe_2O_4$–alginate composite beads, J. Environ. Chem. Eng. 3 (2015) 1486–1496.

[29] S.A. Elfeky, S. Ebrahim Mahmoud, A. Fahmy Youssef, Applications of CTAB modified magnetic nanoparticles for removal of chromium (VI) from contaminated water, J. Adv. Res. 8(4) (2017) 435–443.

[30] R. Darvishi Cheshmeh Soltani, G. Shams Khorramabadi, A.R. Khataee, S. Jorfi, Silica nanopowders/alginate composite for adsorption of lead (II) ions in aqueous solutions, J. Taiwan Inst. Chem. Eng. 45 (2014) 973–980.

[31] R.D.C. Soltani, A. Rezaee, H. Godini, A.R. Khataee, A. Hasanbeiki, Photoelectrochemical treatment of ammonium using seawater as a natural supporting electrolyte, Chem. Ecol. 29 (2013) 72-85.

[32] M. El kady, H. Shokry, H. Hamad, Effect of superparamagnetic nanoparticles on the physicochemical properties of nano hydroxyapatite for groundwater treatment: Adsorption mechanism of Fe(II) and Mn (II), RSC Adv. 6 (2016) 82244-82259.

[33] A. Mohseni-Bandpi, B. Kakavandi, R.R. Kalantary, A. Azari, A. Keramati, Development of a novel magnetite-chitosan composite for the removal of fluoride from drinking water: Adsorption modeling and optimization, RSC Adv.5 (2015) 73279-73289.

[34] H. Shekari, M.H. Sayadi, M.R. Rezaei, A. Allahresani, Synthesis of nickel ferrite/titanium oxide magnetic nanocomposite and its use to remove hexavalent chromium from aqueous solutions, Surf. Interface. 8 (2017) 199-205.

[35] K.S. Padmavathy, G. Madhu, P.V. Haseena, A study on effects of pH, adsorbent dosage, time, initial concentration and adsorption isotherm study for the removal of hexavalent chromium (Cr (VI)) from wastewater by magnetite nanoparticles, Procedia Technol. 24 (2016) 585–594.

[36] S.C.W. Sakti, Y. Narita, T. Sasaki, Nuryono, S. Tanaka, A novel pyridinium functionalized magnetic chitosan with pH-independent and rapid adsorption kinetics for magnetic separation of Cr(VI), J. Environ. Chem. Eng. 3 (2015) 1953-1961.

[37] H. Javadian, P. Vahedian, M. Toosi, Adsorption characteristics of Ni(II) from aqueous solution and industrial wastewater onto Polyaniline/HMS nanocomposite powder, Appl. Surf. Sci. 284 (2013) 13-22.

[38] V.S. Munagapati, D.S. Kim, Equilibrium isotherms, kinetics, and thermodynamics studies for congo red adsorption using calcium alginate beads impregnated with nano-goethite, Ecotoxicol. Environ. Saf. 141 (2017) 226–234.

[39] H. Javadian, M. Torabi Angaji, M. Naushad, Synthesis and characterization of polyaniline/γ-alumina nanocomposite: A comparative study for the adsorption of three different anionic dyes, J. Ind. Eng. Chem. 20 (2014) 3890-3900.

[40] S. Malamis, E. Katsou, A review on zinc and nickel adsorption on natural and modified zeolite, bentonite and vermiculite: examination of process parameters, kinetics and isotherms. J. Hazard. Mater. 252 (2013) 428–461.

[41] F.F. Zeng, Y. He, Z.H. Lian, J.M. Xu, The impact of solution chemistry of electrolyte on the sorption of pentachlorophenol and phenanthrene by natural hematite nanoparticles. Sci. Total Environ. 466 (2014) 577–585.

Table 1. CCD levels, experimental design and the responses.

Symbol	Factors	Unit	Levels				
			-α (-2)	Low (-1)	Central (0)	High (1)	+α (+2)
X_1	Contact time	min	2	19	36	53	70
X_2	Adsorbent dosage	g	0.05	0.125	0.2	0.275	0.35
X_3	Nd (III) concentration	mg/L	30	45	60	75	90
X_4	Tb (III) concentration	mg/L	30	45	60	75	90
X_5	Dy (III) concentration	mg/L	30	45	60	75	90

Run	Factors					Nd adsorption efficiency (%)		Tb adsorption efficiency (%)		Dy adsorption efficiency (%)	
	X1	X2	X3	X4	X5	Observed	Predicated	Observed	Predicated	Observed	Predicated
1	36	0.2	60	60	30	90.76	90.92	95.85	96.19	97.53	98.38
2	53	0.275	75	75	75	94.56	95.81	96.87	97.99	98.11	99.49
3	36	0.2	90	60	60	87.96	86.97	90.53	89.74	92.89	92.17

4(C)	36	0.2	60	60	60	91.45	91.56	94.03	93.83	95.75	95.59
5	19	0.125	45	45	75	67.08	65.91	70.16	68.76	73.17	71.86
6	36	0.2	60	90	60	89.7	90.18	91.64	91.83	92.85	92.90
7	19	0.125	75	75	75	54.56	53.65	57.87	57.07	59.06	58.32
8	19	0.125	75	45	45	62.65	61.90	67.59	66.71	72.45	71.31
9	70	0.2	60	60	60	88.12	86.43	90.56	88.55	92.92	90.59
10	53	0.125	75	75	45	71.98	71.84	77.64	77.97	79.51	79.74
11(C^{*})	36	0.2	60	60	60	91.97	91.56	94.46	93.83	96.01	95.59
12	2	0.2	60	60	60	65.78	67.47	67.73	70.34	69.45	72.25
13	53	0.275	75	45	45	92.56	93.97	95.54	96.59	97.98	98.96
14	19	0.275	75	45	75	89.1	89.74	91.94	91.86	95.7	95.71
15	53	0.125	45	45	45	87.6	87.20	90.19	89.92	92.85	92.51
16	36	0.2	30	60	60	94.46	95.45	96.21	97.60	98.25	99.45
17(C)	36	0.2	60	60	60	91.72	91.56	94.09	93.83	95.71	95.59
18(C)	36	0.2	60	60	60	90.96	91.56	93.52	93.83	95.35	95.59
19(C)	36	0.2	60	60	60	91.58	91.56	93.85	93.83	95.32	95.59

20	36	0.2	60	30	60	95.64	95.16	94.43	94.84	98.65	99.07
21	19	0.275	45	45	45	92.75	92.82	94.74	94.09	97.54	96.76
22	53	0.275	45	75	45	94.56	95.23	96.44	97.00	98.45	99.05
23	19	0.275	75	75	45	92.49	92.81	94.63	94.58	96.2	95.99
24	53	0.125	45	75	75	76.01	75.45	79.06	78.86	81.63	81.69
25	19	0.125	45	75	45	59.07	57.58	68.72	67.35	69.38	67.85
26(C)	36	0.2	60	60	60	91.7	91.56	93.65	93.83	95.9	95.59
27	53	0.125	75	45	75	65.46	65.63	72.26	72.55	76.16	76.61
28	19	0.275	45	75	75	90.07	89.98	94.78	94.21	96.59	96.21
29	53	0.275	45	45	75	94.11	95.10	96.07	96.59	98.5	99.31
30	36	0.05	60	60	60	35.32	37.94	45.19	47.04	47.59	49.51
31	36	0.35	60	60	60	92.14	89.52	94.22	92.97	96.36	94.91
32	36	0.2	60	60	90	85.56	85.40	89.35	89.61	93.01	92.63

*Central point

Table 2. ANOVA results for adsorption of the ions by the CA/CMC/$Ni_{0.2}Zn_{0.2}Fe_{2.6}O_4$.

Source	DF[a]	Nd (III)				Tb (III)				Dy (III)			
		SS[b]	MS[c]	F-Value	P-value	SS[b]	MS[c]	F-Value	P-value	SS[b]	MS[c]	F-Value	P-value
Model	20	6816.27	340.81	111.8	<0.0001	5455.58	272.78	104.63	0.0001 <	5394.59	269.73	88.64	<0.0001
X_1	1	539.13	539.13	176.86	0.0001 <	497.77	497.77	190.92	0.0001 <	504.53	504.53	165.81	0.0001 <
X_1^2	1	391.55	391.55	128.45	0.0001 <	379.51	379.51	145.56	0.0001 <	368.18	368.18	121	0.0001 <
X_2	1	3989.46	3989.46	1308.75	0.0001 <	3164.35	3164.35	1213.69	0.0001 <	3091.74	3091.74	1016.05	0.0001 <
X_2^2	1	1420.35	1420.35	465.95	0.0001 <	1040.89	1040.89	399.24	0.0001 <	1002.26	1002.26	329.38	0.0001 <
X_3	1	107.91	107.91	35.40	0.0001 <	92.75	92.75	35.57	0.0001 <	79.42	79.42	26.10	0.0003
X_3^2	1	0.23	0.23	0.075	0.7887	0.049	0.049	0.019	0.8939	0.084	0.084	0.027	0.8713
X_4	1	37.23	37.23	12.21	0.0050	13.59	13.59	5.21	0.0433	57.10	57.10	18.77	0.0012
X_4^2	1	2.24	2.24	0.74	0.4094	0.45	0.45	0.17	0.6844	0.28	0.28	0.093	0.7657
X_5	1	45.68	45.68	14.98	0.0026	64.94	64.94	24.91	0.0004	49.54	49.54	16.28	0.0020
X_5^2	1	21.24	21.24	6.97	0.0230	1.59	1.59	0.61	0.4506	0.014	0.014	0.00449	0.9478
X_1X_2	1	134.04	134.04	43.97	0.0001 <	132.14	132.14	50.68	0.0001 <	150.55	150.55	49.48	0.0001 <
X_1X_3	1	19.25	19.25	6.32	0.0288	0.59	0.59	0.23	0.6428	2.56	2.56	0.84	0.3787
X_1X_4	1	10.19	10.19	3.34	0.0947	1.2	1.2	0.46	0.5117	6.05	6.05	1.99	0.1861
X_1X_5	1	6.77	6.77	2.22	0.1642	1.33	1.33	0.51	0.4893	0.7	0.7	0.23	0.6415
X_2X_3	1	65.33	65.33	21.43	0.0007	55.2	55.2	21.17	0.0008	44.76	44.76	14.71	0.0028
X_2X_4	1	37.00	37.00	12.14	0.0051	28.46	28.46	10.92	0.0070	38.07	38.07	12.51	0.0047
X_2X_5	1	11.68	11.68	3.83	0.0762	33.35	33.35	12.79	0.0043	32.78	32.78	10.77	0.0073
X_3X_4	1	41.12	41.12	13.49	0.0037	8.76	8.76	3.36	0.0940	2.72	2.72	0.89	0.3645
X_3X_5	1	5.39	5.39	1.77	0.2104	2.59	2.59	0.99	0.3401	4.82	4.82	1.58	0.2343
X_4X_5	1	17.87	17.87	5.86	0.0339	4.82	4.82	1.85	0.2012	5.22	5.22	1.72	0.2169
Residual	11	33.53	3.05			28.68	2.61			33.47	3.04		
Lack of Fit	6	32.95	5.49	46.87	0.0003	28.11	4.68	41.14	0.0004	33.07	5.51	68.67	0.0001
Pure Error	5	0.59	0.12			0.57	0.11			0.4	0.08		
Cor. Total	31	6849.80				5484.26				5428.06			

R^2=0.9951 AP[d]=40.91	R_{adj}^2=0.9862 C.V. %=2.10	R^2=0.9948 AP[d]=38.95	R_{adj}^2=0.9853 C.V. %=1.87	R^2=0.9938 AP[d]=35.37	R_{adj}^2=0.9826 C.V. %=1.97

[a] Degree of Freedom

[b] Sum of Square

[c] Mean Square

[d] Adequate precision

Table 3. Confirmation experiments for the ions adsorption onto the CA/CMC/$Ni_{0.2}Zn_{0.2}Fe_{2.6}O_4$.

No.	Condition					Nd (III)		Tb (III)		Dy (III)		Error (%)		
	Time (min)	Adsorbent dosage (g)	Initial concentration (mg/L)			Observed	Predicted	Observed	Predicted	Observed	Predicted			
			Nd (III)	Tb (III)	Dy (III)							Nd (III)	Tb (III)	Dy (III)
1	53	0.1	30	30	30	94.61	95.72	96.73	96.17	98.83	99.44	1.17	0.58	0.61
2	19	0.125	75	45	45	63.12	61.9	68.27	66.71	72.85	71.31	1.93	2.28	2.11
3	36	0.2	90	60	60	87.44	86.97	90.86	89.74	93.73	92.17	0.54	1.23	1.66
4	53	0.275	45	75	45	93.48	95.23	96.18	97	97.54	99.05	1.87	0.85	1.54

Table 4. Kinetic constants for adsorption of Nd (III), Tb (III), and Dy (III) by the CA/CMC/$Ni_{0.2}Zn_{0.2}Fe_{2.6}O_4$.

		Nd (III)	Tb (III)	Dy (III)
PFO	K_1 (1/min)	0.2905	0.290	0.289
	q_e (mg/g)	15.07	15.30	15.61
	R^2	0.9617	0.9585	0.9587
	□^{2}	0.240	0.268	0.279
PSO	K_2 (g/mg min) × 10^2	2.99	2.93	2.86
	q_e (mg/g)	16.15	16.40	16.74
	h (mg/g min) × 10^{-2}	7.79	7.88	8.01
	R^2	0.9927	0.9933	0.9929
	□^{2}	0.045	0.043	0.048
IPD	K_i (1/min)	3.88	3.96	4.05
	R^2	0.8157	0.8225	0.8222
	□^{2}	1.16	1.15	1.20

Table 5. Isotherm constants for adsorption of Nd (III), Tb (III), and Dy (III) by the CA/CMC/$Ni_{0.2}Zn_{0.2}Fe_{2.6}O_4$.

		Nd (III)	Tb (III)	Dy (III)
Langmuir	b (L/mg)	0.78	0.89	1.27
	q_m (mg/g)	23.15	24.41	25.24
	R^2	0.8773	0.9238	0.9125
	□^{2}	1.62	1.21	1.61
Freundlich	K ($mg^{1-1/n}$ $L^{1/n}$/g)	14.40	15.46	16.49
	n	9	9.26	9.71
	R^2	0.9879	0.9654	0.9633
	□^{2}	0.159	0.55	0.675

Table 6. Effect of temperature on the adsorption of Nd (III), Tb (III), and Dy (III) at 90 mg/L and thermodynamic parameters.

Temperature (°C)	Adsorption efficiency (%)		
	Nd (III)	Tb (III)	Dy (III)
25	44.31	47.14	49.21
35	48.23	50.48	53.45
45	52.64	55.99	58.42
Thermodynamic parameters			
	Nd (III)	Tb (III)	Dy (III)
ΔH° (kJ/mol)	13.9	14.76	15.45
ΔS° (kJ/mol K)	0.039	0.043	0.046
Temperature (°C)			
25	2.022	1.739	1.534
35	1.686	1.408	1.151
45	1.274	0.918	0.655

Table 7. Parameters of breakthrough and the values predicted by Thomas and Yan models.

Metal	Breakthrough analysis			Thomas model			Yan model		
	q_e	Adsorption efficiency (%)	C_e	$K_{Th} \times 10^4$	q_e	R^2	q_e	a	R^2
Nd (III)	22.70	46.33	16.10	5.65	22.18	0.9945	21.10	3.74	0.9957
Tb (III)	24.00	47.07	15.88	5.52	23.44	0.9937	22.32	3.83	0.9962
Dy (III)	25.54	49.11	15.26	5.46	24.96	0.9940	23.92	4.01	0.9970

Fig. 1. (A) XRD pattern of $Ni_{0.2}Zn_{0.2}Fe_{2.6}O_4$ nanopartciles; Photo of $Ni_{0.2}Zn_{0.2}Fe_{2.6}O_4$ nanoparticles (B) before drying and (C) in the solution under magnetic field after drying.

Fig. 2. FE-SEM images of (A) $Ni_{0.2}Zn_{0.2}Fe_{2.6}O_4$ and (B) CA/CMC/$Ni_{0.2}Zn_{0.2}Fe_{2.6}O_4$.

Fig. 3. FT-IR spectra of (A) CA, (B) CMC, (C) $Ni_{0.2}Zn_{0.2}Fe_{2.6}O_4$, and (D) CA/CMC/$Ni_{0.2}Zn_{0.2}Fe_{2.6}O_4$.

Fig. 4. (A) N_2 adsorption−desorption isotherm and (B) pore size distributions of the synthesized CA/CMC/$Ni_{0.2}Zn_{0.2}Fe_{2.6}O_4$.

Fig. 5. EDX spectra of (A) $Ni_{0.2}Zn_{0.2}Fe_{2.6}O_4$ and (B) CA/CMC/$Ni_{0.2}Zn_{0.2}Fe_{2.6}O_4$, and (C) CA/CMC/$Ni_{0.2}Zn_{0.2}Fe_{2.6}O_4$ after adsorption of the ions.

Fig. 6. TGA curve of CA/CMC/$Ni_{0.2}Zn_{0.2}Fe_{2.6}O_4$.

Fig. 7. Magnetization curves of (A) $Ni_{0.2}Zn_{0.2}Fe_{2.6}O_4$ and (B) CA/CMC/$Ni_{0.2}Zn_{0.2}Fe_{2.6}O_4$; (C) Magnetic separation of the ions-loaded adsorbent.

Fig. 8. Effects of pH on the adsorption of the ions.

Fig. 9. Normal probability plots of residuals for the ions adsorption.

Fig. 10. Plots of studentized residuals versus predicted for the ions adsorption.

Fig. 11. Plots of studentized residuals versus experimental run number for the ions.

Fig. 12. 3D response surface plots of the ions adsorption onto CA/CMC/$Ni_{0.2}Zn_{0.2}Fe_{2.6}O_4$.

Fig. 13. (A) Effect of ionic strength on the adsorption of Nd (III), Tb (III), and Dy (III), (B) Ln K_d versus 1/T for calculation of enthalpy and entropy changes, and (C) Reusability of CA/CMC/$Ni_{0.2}Zn_{0.2}Fe_{2.6}O_4$ for adsorption of the ions.

Fig. 14. (A) Experimental data of the column adsorption and (B-D) Modeling of the experimental data with Thomas and Yan models.

Author statement

Hamedreza Javadian: Investigation, Acquisition of data, Analysis and/or interpretation of data, Drafting the manuscript and Revising the manuscript. **Montsserat Ruiz**: Acquisition of data and Supervision. **Ana Maria Sastre**: Conceptualization and supervision.

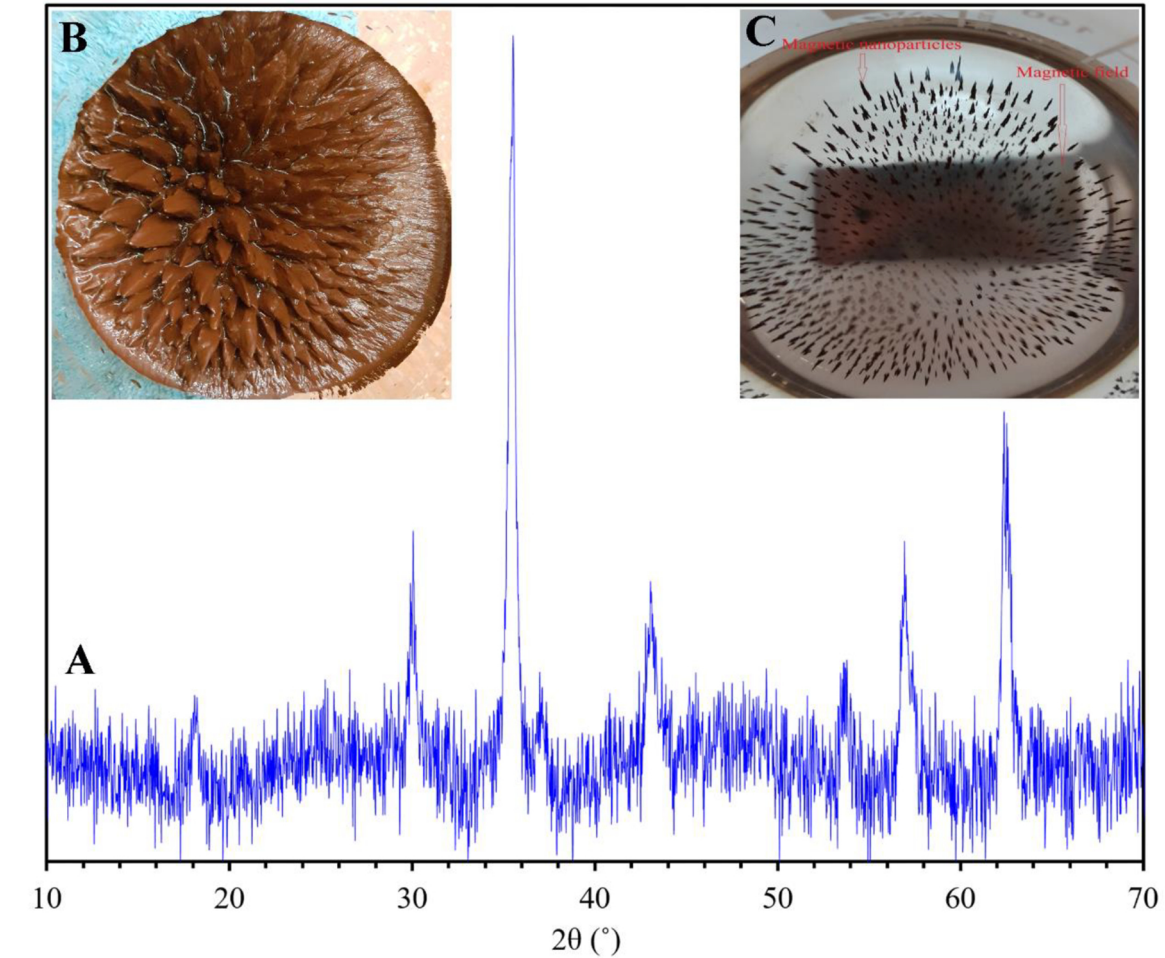
B
C
Magnetic nanoparticles
Magnetic field
A
10
20
30
40
50
60
70
2θ (°)

Figure 1

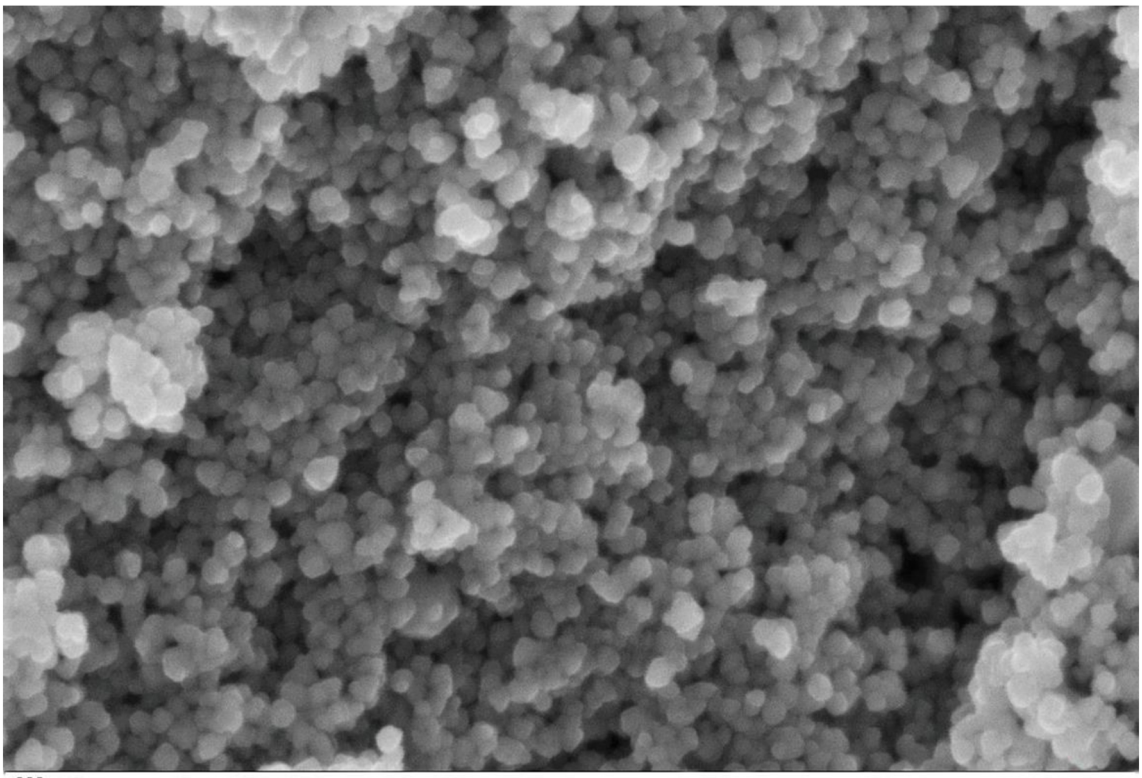
200 nm
Mag = 144.87 K X
WD = 4.5 mm
EHT = 5.00 kV
A

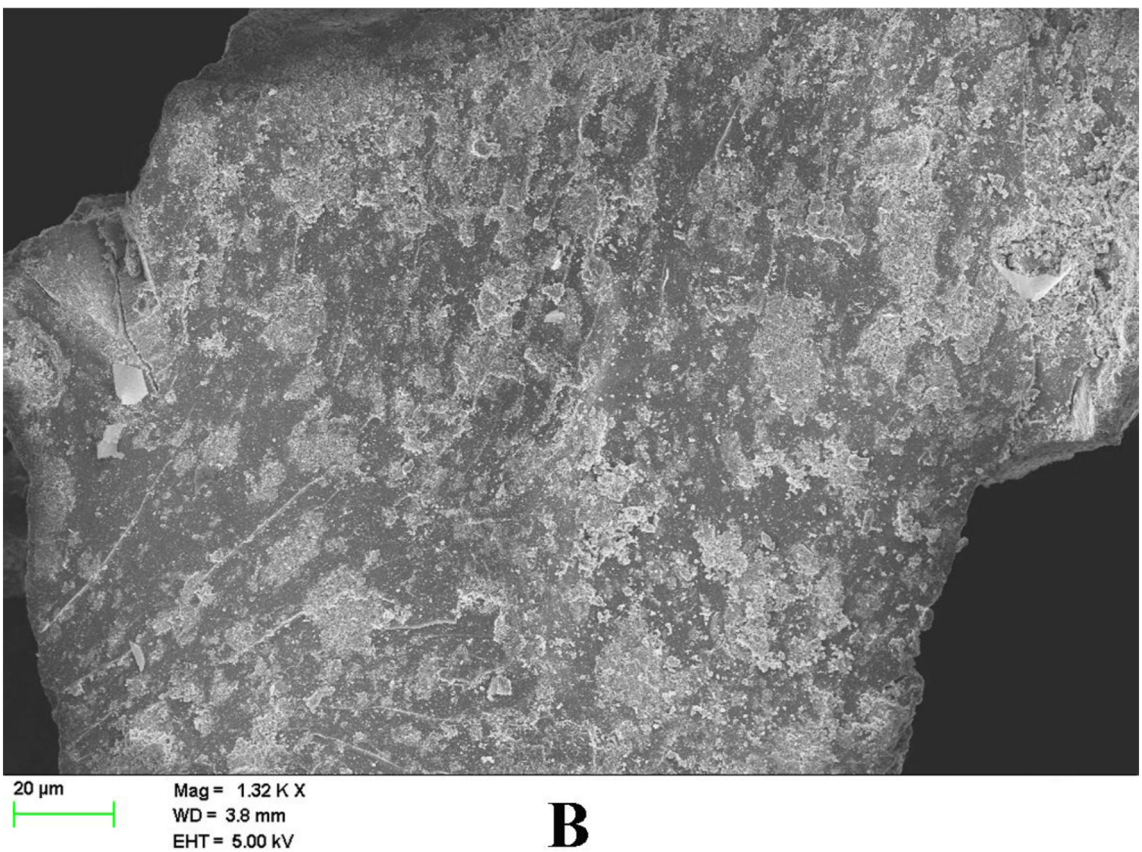
20 µm
Mag = 1.32 K X
WD = 3.8 mm
EHT = 5.00 kV
B

Figure 2

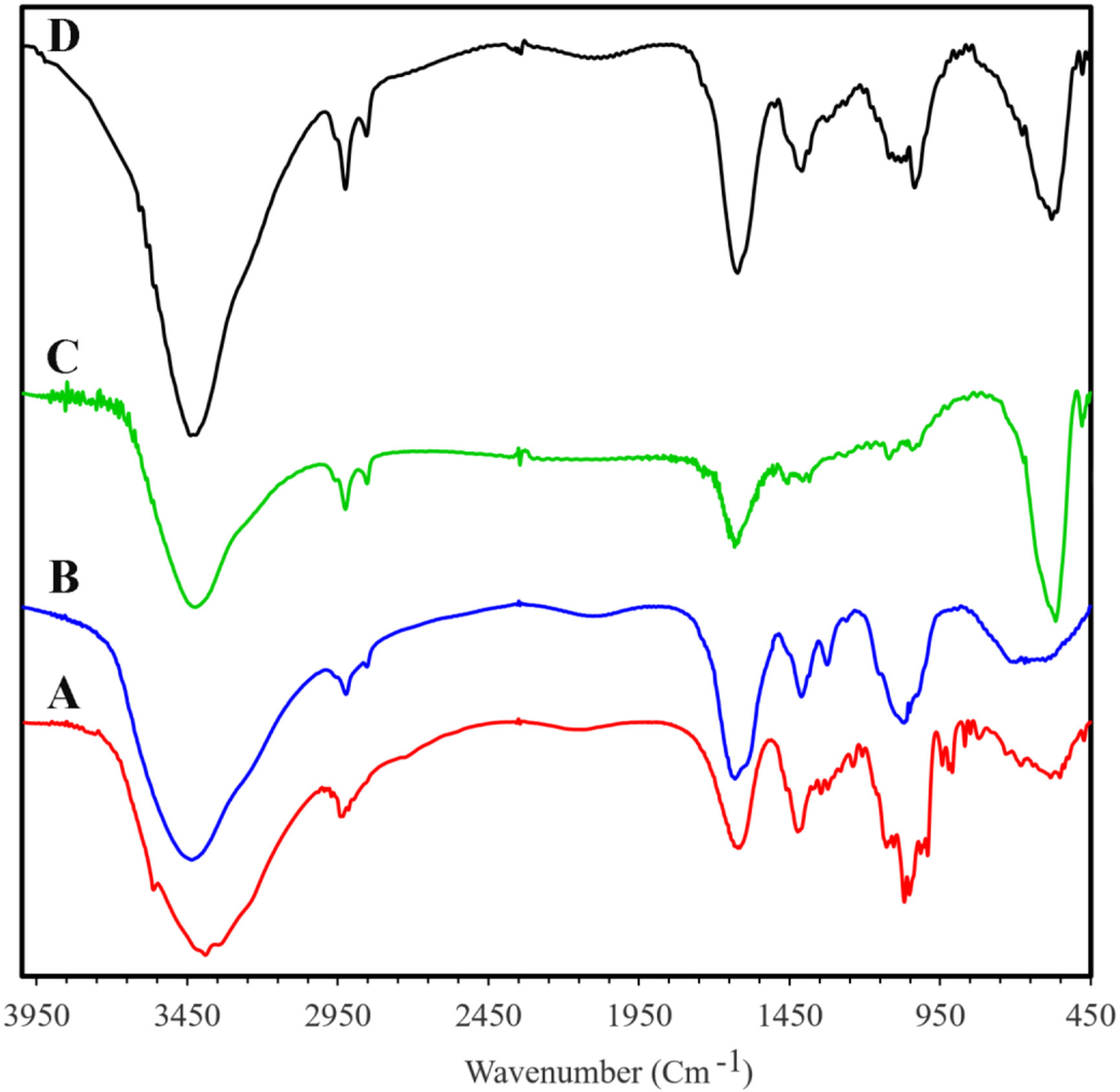

Figure 3

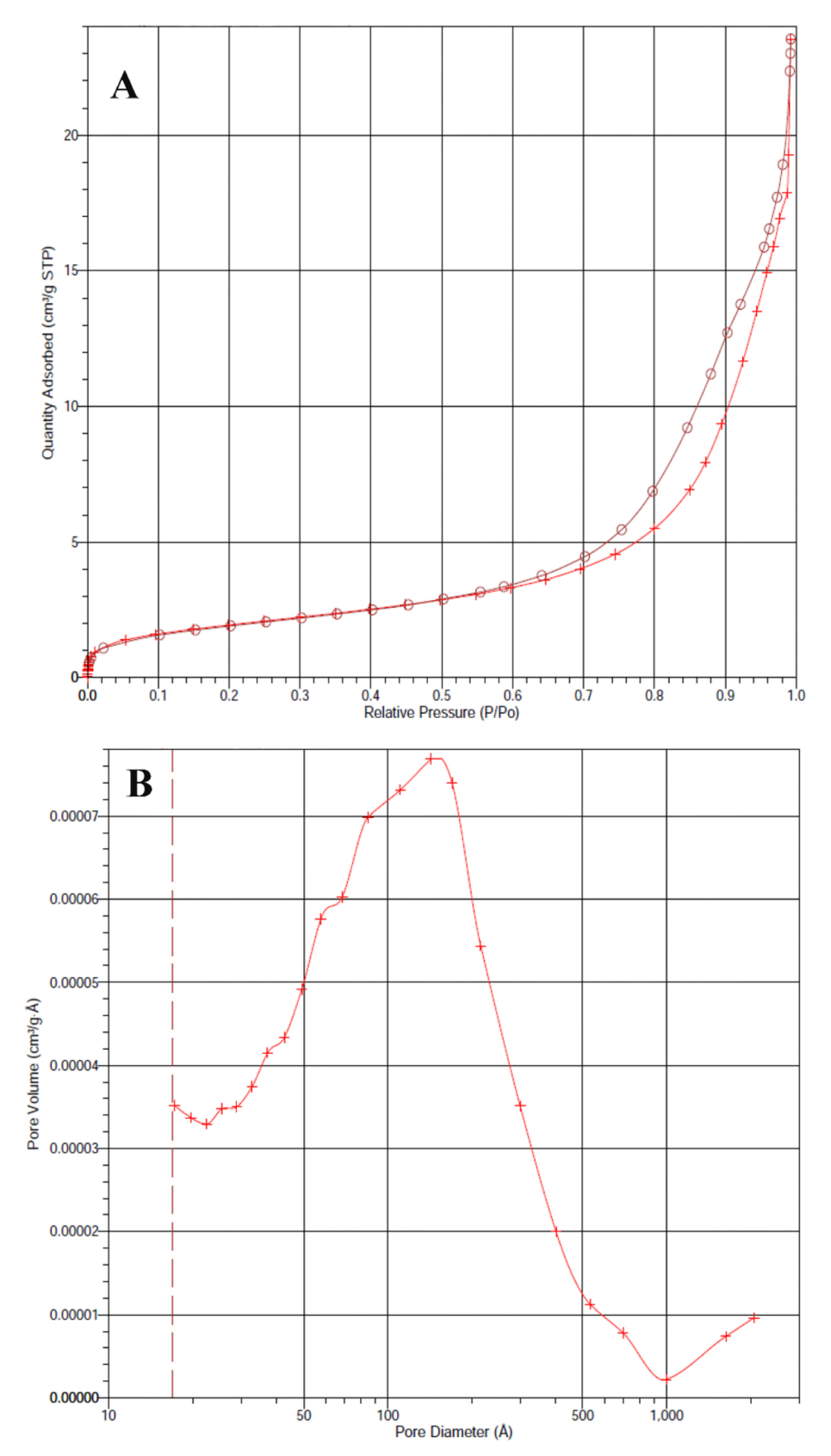
A
Quantity Adsorbed (cm³/g STP)
0
5
10
15
20
0.0
0.1
0.2
0.3
0.4
0.5
0.6
0.7
0.8
0.9
1.0
Relative Pressure (P/Po)
B
Pore Volume (cm³/g·Å)
0.00000
0.00001
0.00002
0.00003
0.00004
0.00005
0.00006
0.00007
10
50
100
500
1,000
Pore Diameter (Å)

Figure 4

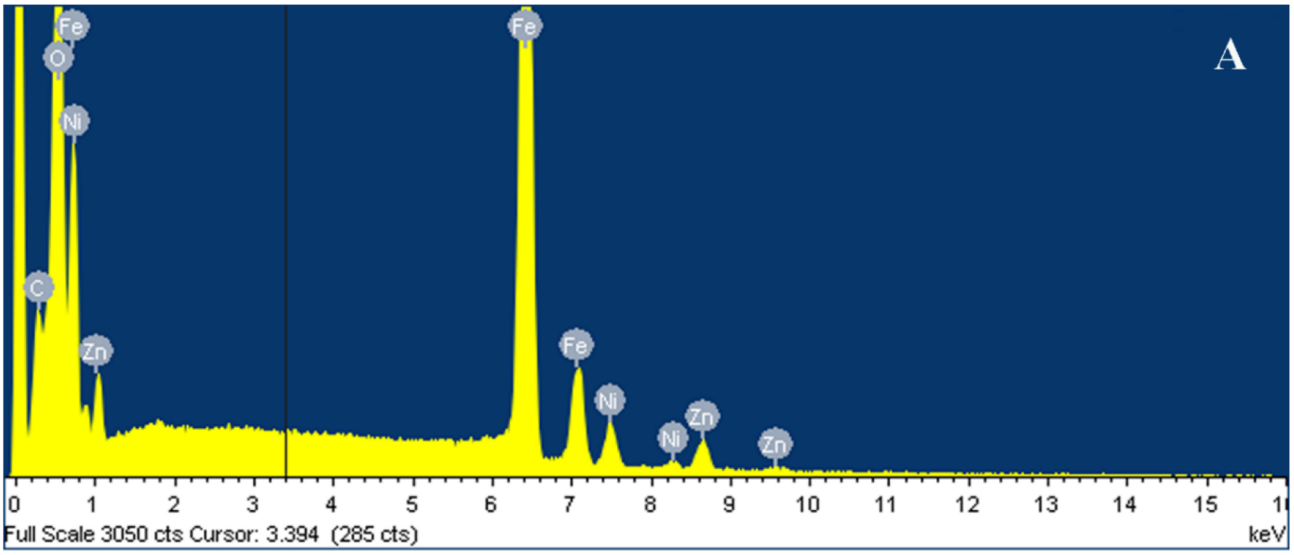
A
Fe
O
Ni
C
Zn
Fe
Fe
Ni
Ni
Zn
Zn
0 1 2 3 4 5 6 7 8 9 10 11 12 13 14 15
Full Scale 3050 cts Cursor: 3.394 (285 cts)
keV

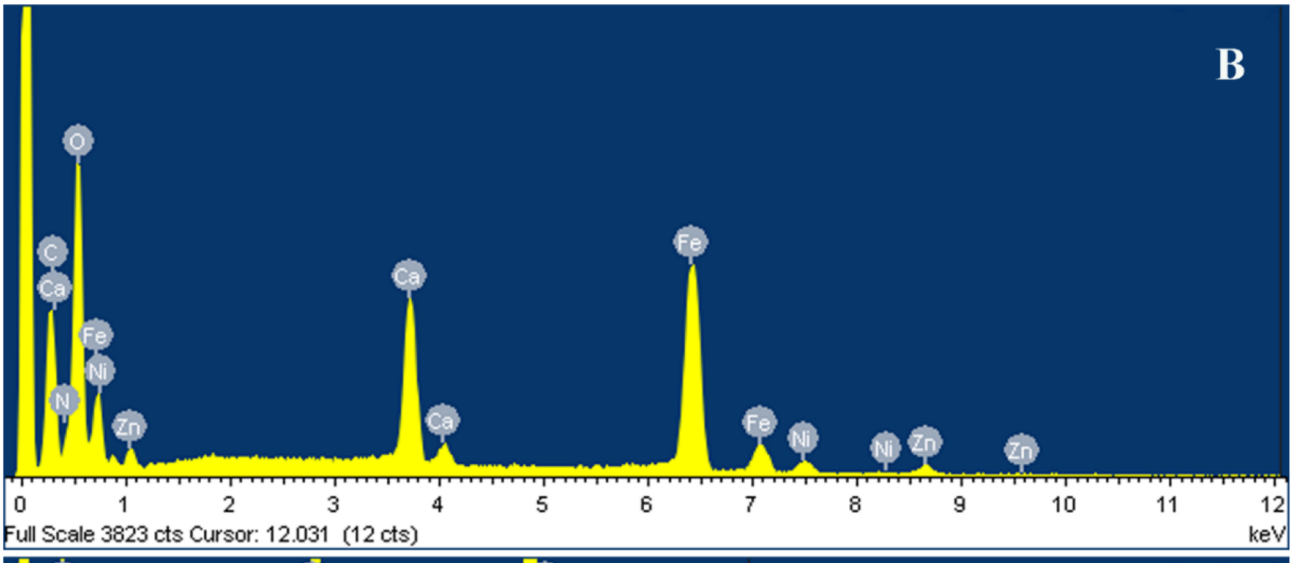
B
O
C
Ca
Fe
Ni
N
Zn
Ca
Ca
Fe
Fe
Ni
Ni
Zn
Zn
0 1 2 3 4 5 6 7 8 9 10 11 12
Full Scale 3823 cts Cursor: 12.031 (12 cts)
keV

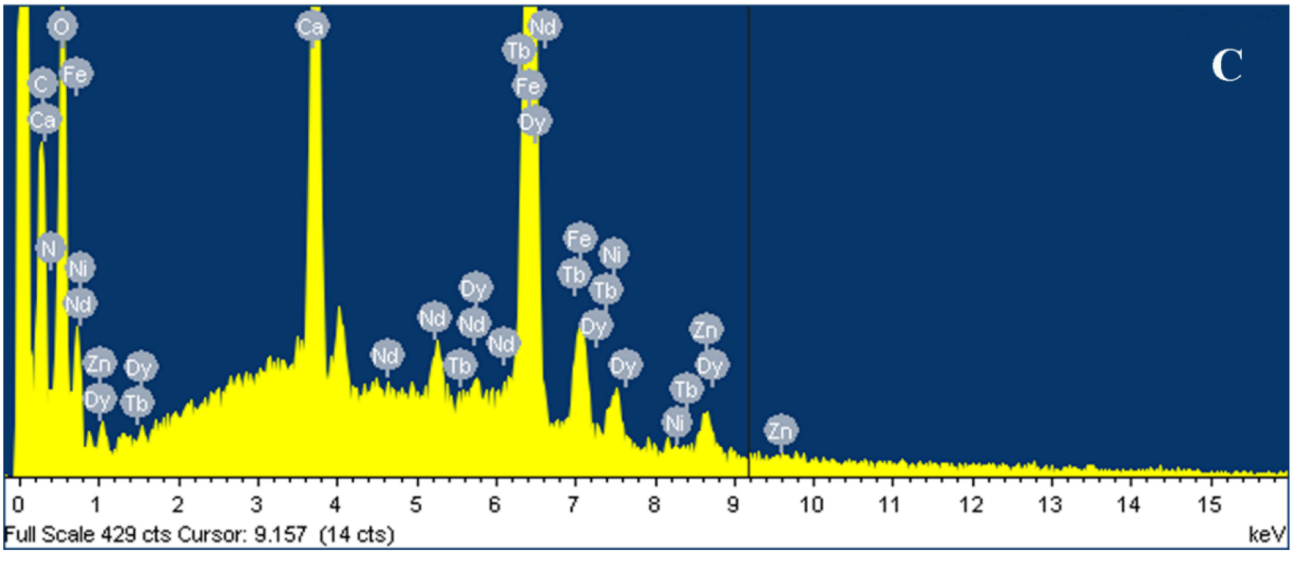
C
O
Fe
C
Ca
N
Ni
Nd
Zn
Dy
Dy
Tb
Ca
Nd
Dy
Nd
Nd
Nd
Tb
Nd
Tb
Fe
Dy
Fe
Ni
Tb
Tb
Dy
Dy
Zn
Dy
Tb
Ni
Zn
0 1 2 3 4 5 6 7 8 9 10 11 12 13 14 15
Full Scale 429 cts Cursor: 9.157 (14 cts)
keV

Figure 5

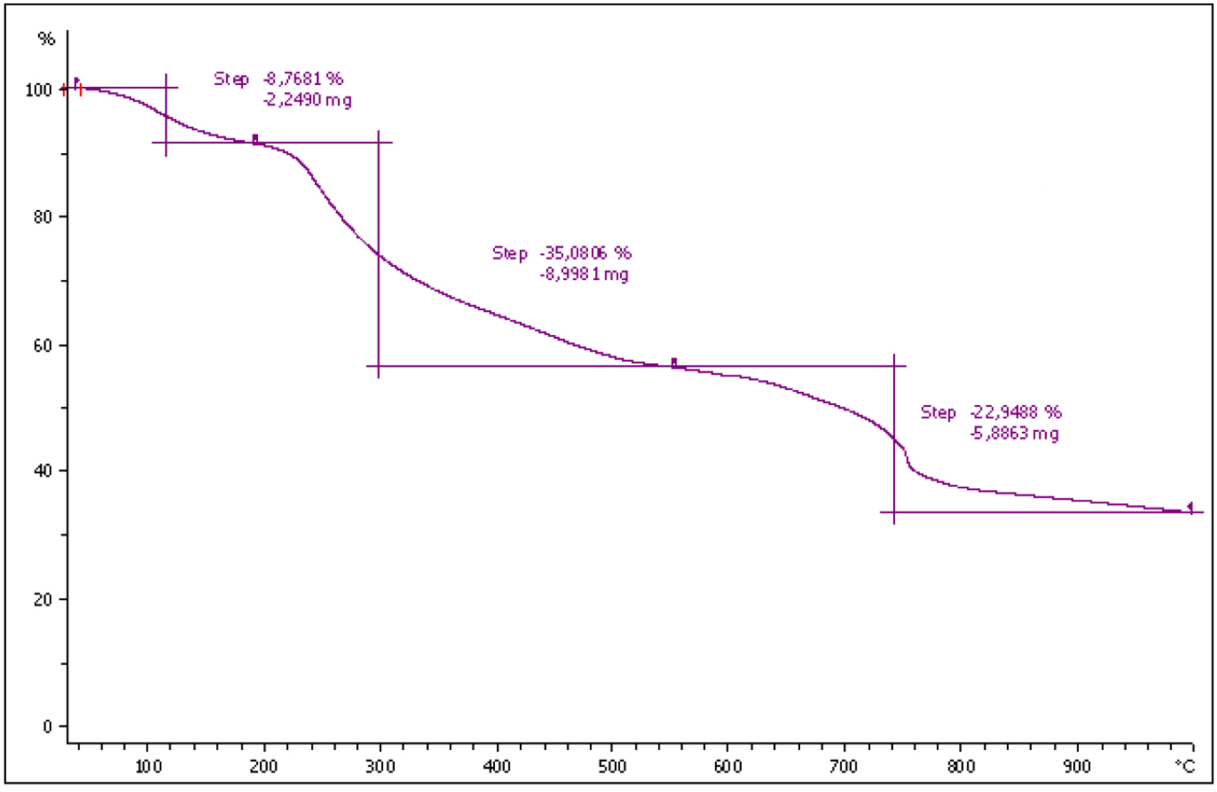
%
100
80
60
40
20
0
Step -8,7681 %
-2,2490 mg
Step -35,0806 %
-8,9981 mg
Step -22,9488 %
-5,8863 mg
100
200
300
400
500
600
700
800
900
°C

Figure 6

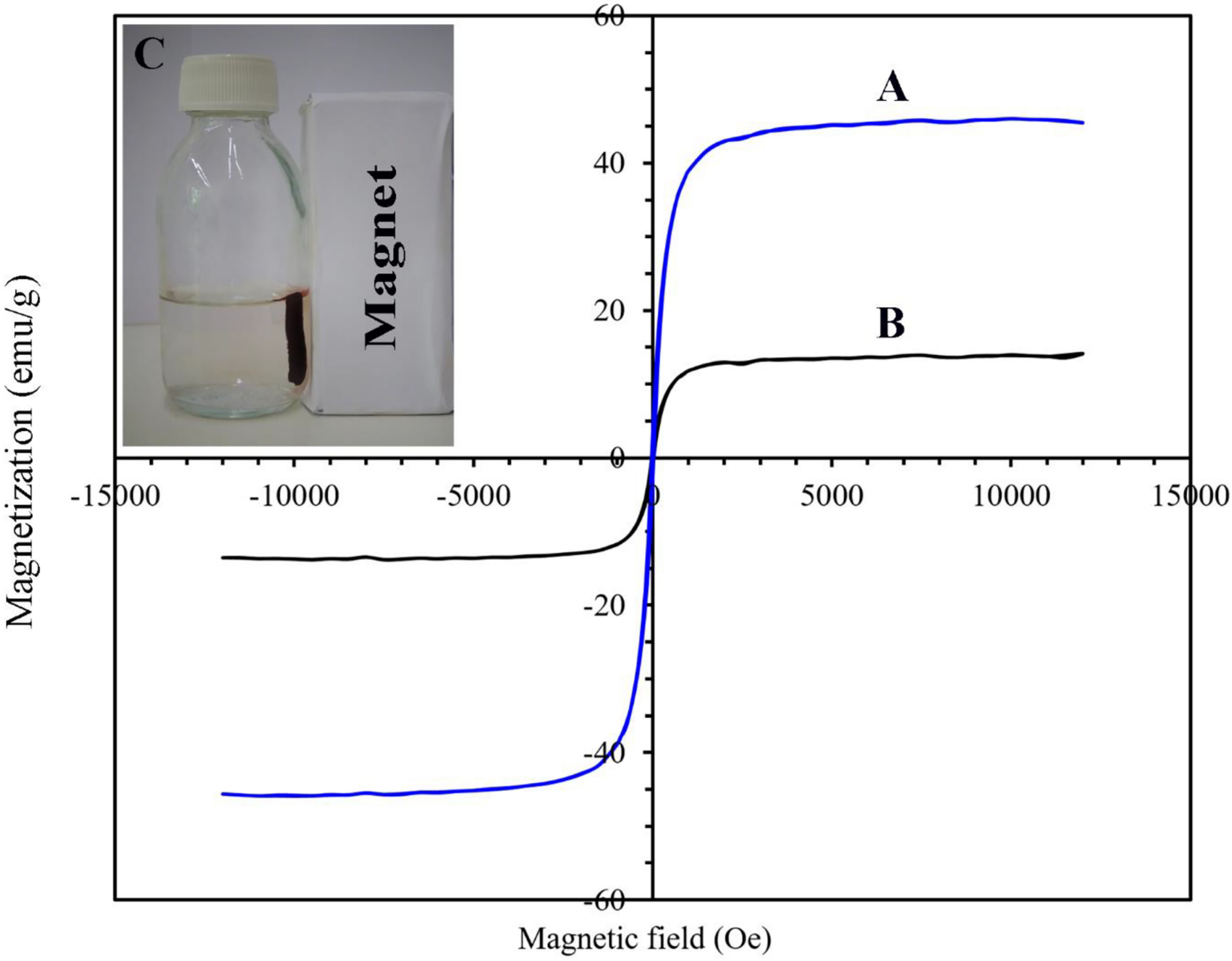
C
Magnet
A
B
60
40
20
0
-20
-40
-60
-15000
-10000
-5000
5000
10000
15000
Magnetization (emu/g)
Magnetic field (Oe)

Figure 7

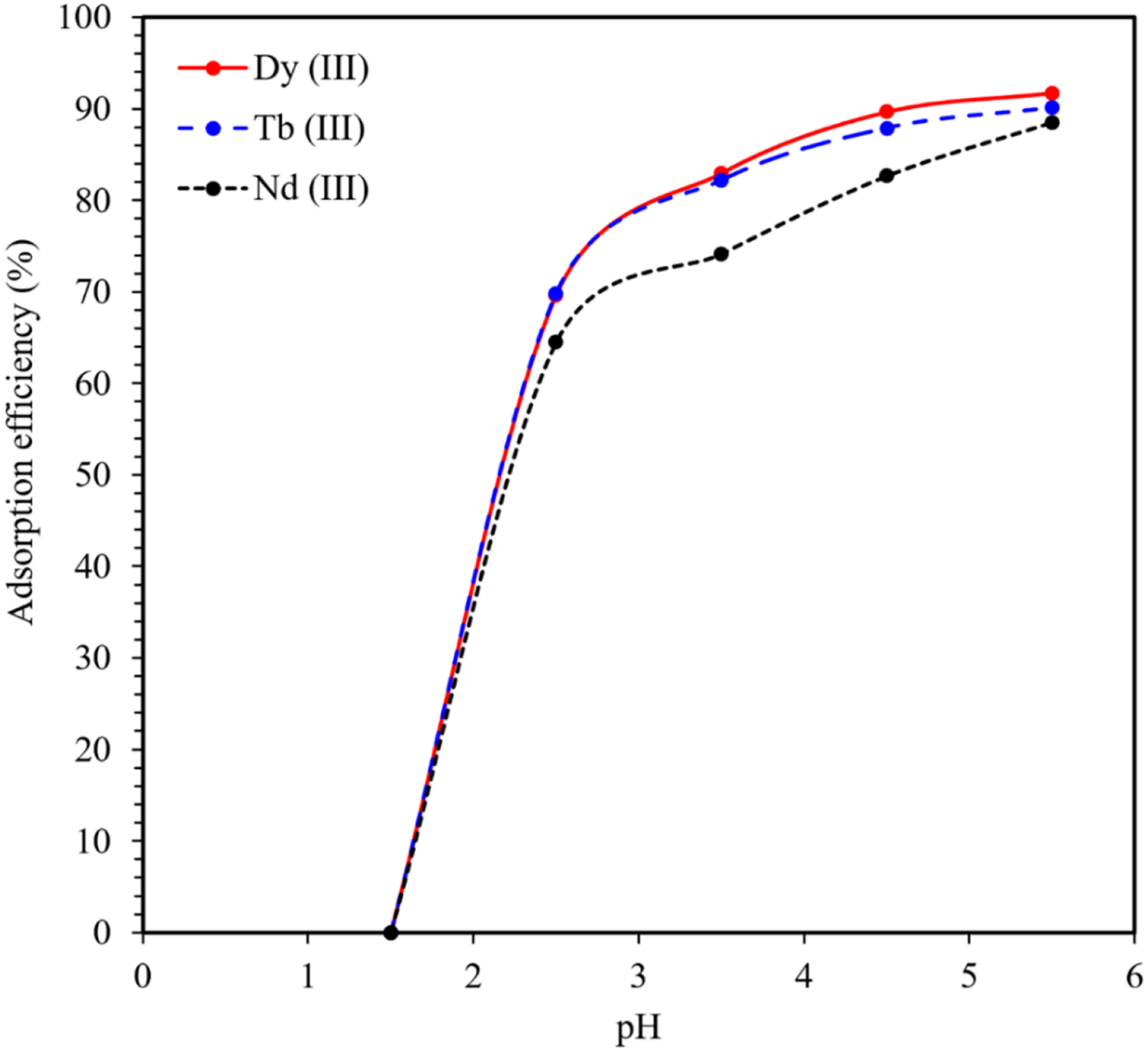
Dy (III)
Tb (III)
Nd (III)
Adsorption efficiency (%)
pH
0
10
20
30
40
50
60
70
80
90
100
0
1
2
3
4
5
6

Figure 8

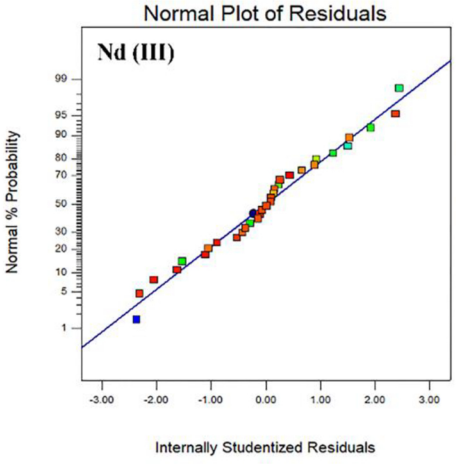
Normal Plot of Residuals
Nd (III)
Normal % Probability
99
95
90
80
70
50
30
20
10
5
1
-3.00
-2.00
-1.00
0.00
1.00
2.00
3.00
Internally Studentized Residuals

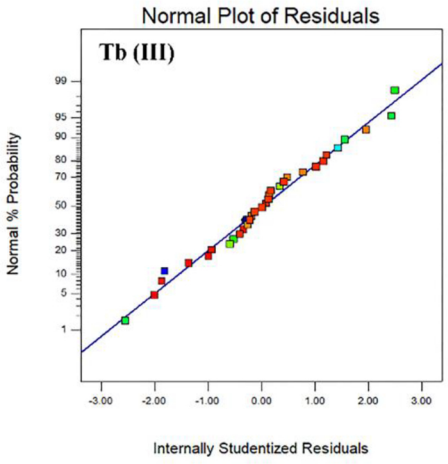
Normal Plot of Residuals
Tb (III)
Normal % Probability
99
95
90
80
70
50
30
20
10
5
1
-3.00
-2.00
-1.00
0.00
1.00
2.00
3.00
Internally Studentized Residuals

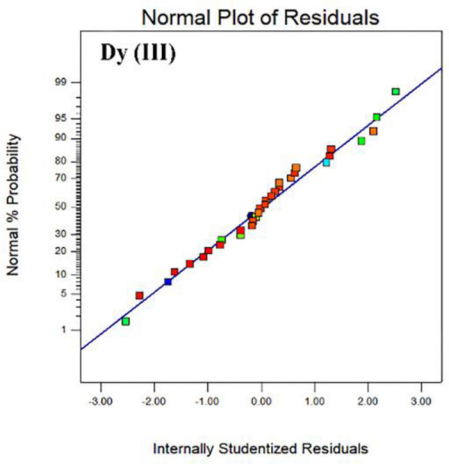
Normal Plot of Residuals
Dy (III)
Normal % Probability
99
95
90
80
70
50
30
20
10
5
1
-3.00
-2.00
-1.00
0.00
1.00
2.00
3.00
Internally Studentized Residuals

Figure 9

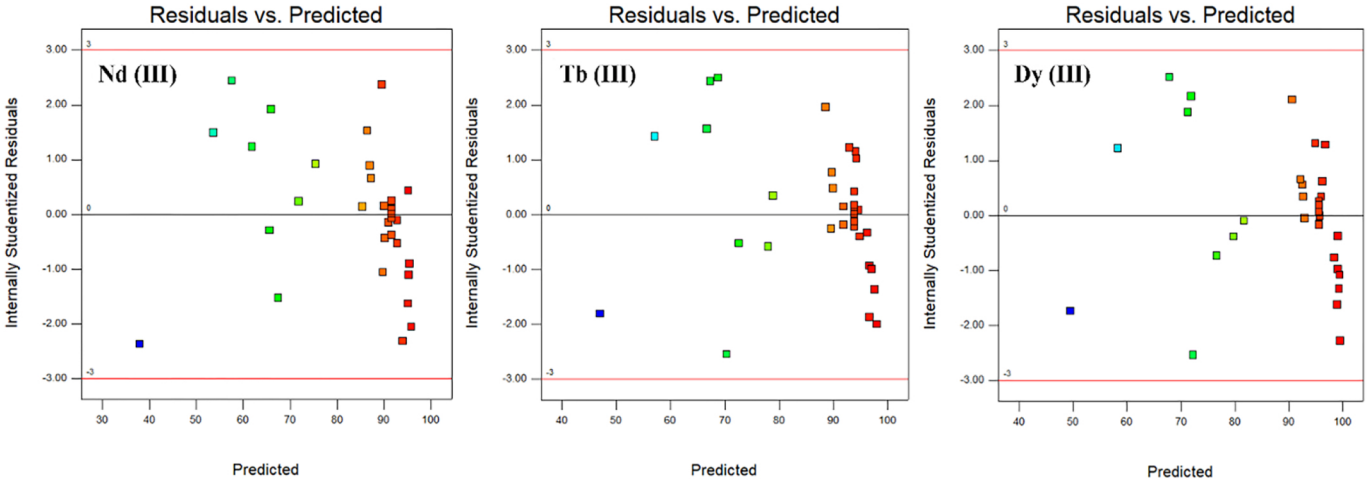
Residuals vs. Predicted
Nd (III)
Internally Studentized Residuals
Predicted
Residuals vs. Predicted
Tb (III)
Internally Studentized Residuals
Predicted
Residuals vs. Predicted
Dy (III)
Internally Studentized Residuals
Predicted

Figure 10

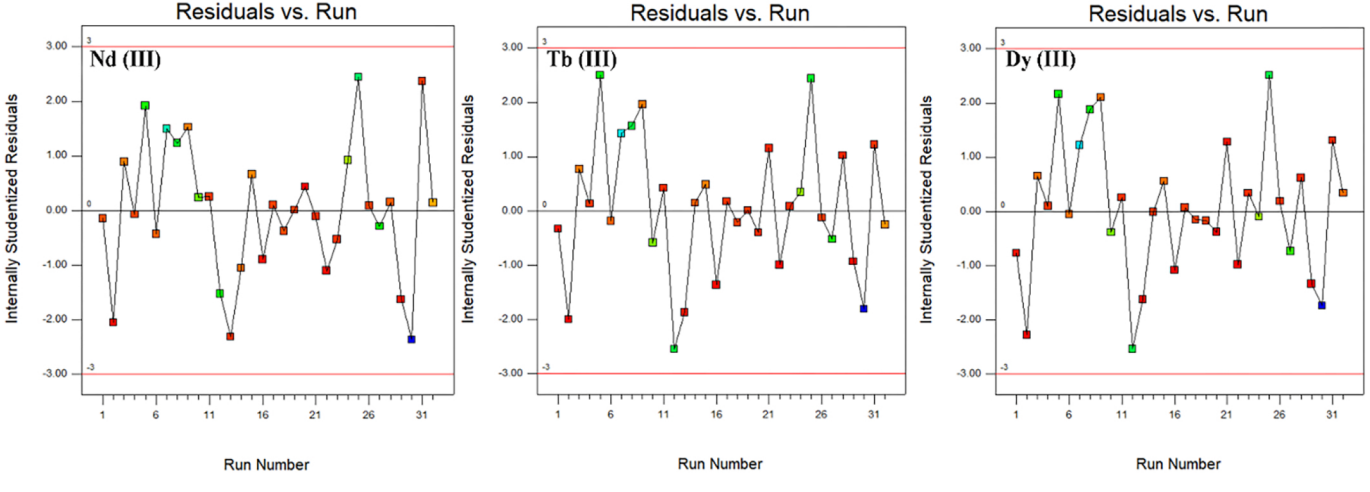
Residuals vs. Run
Nd (III)
Internally Studentized Residuals
Run Number
Residuals vs. Run
Tb (III)
Internally Studentized Residuals
Run Number
Residuals vs. Run
Dy (III)
Internally Studentized Residuals
Run Number

Figure 11

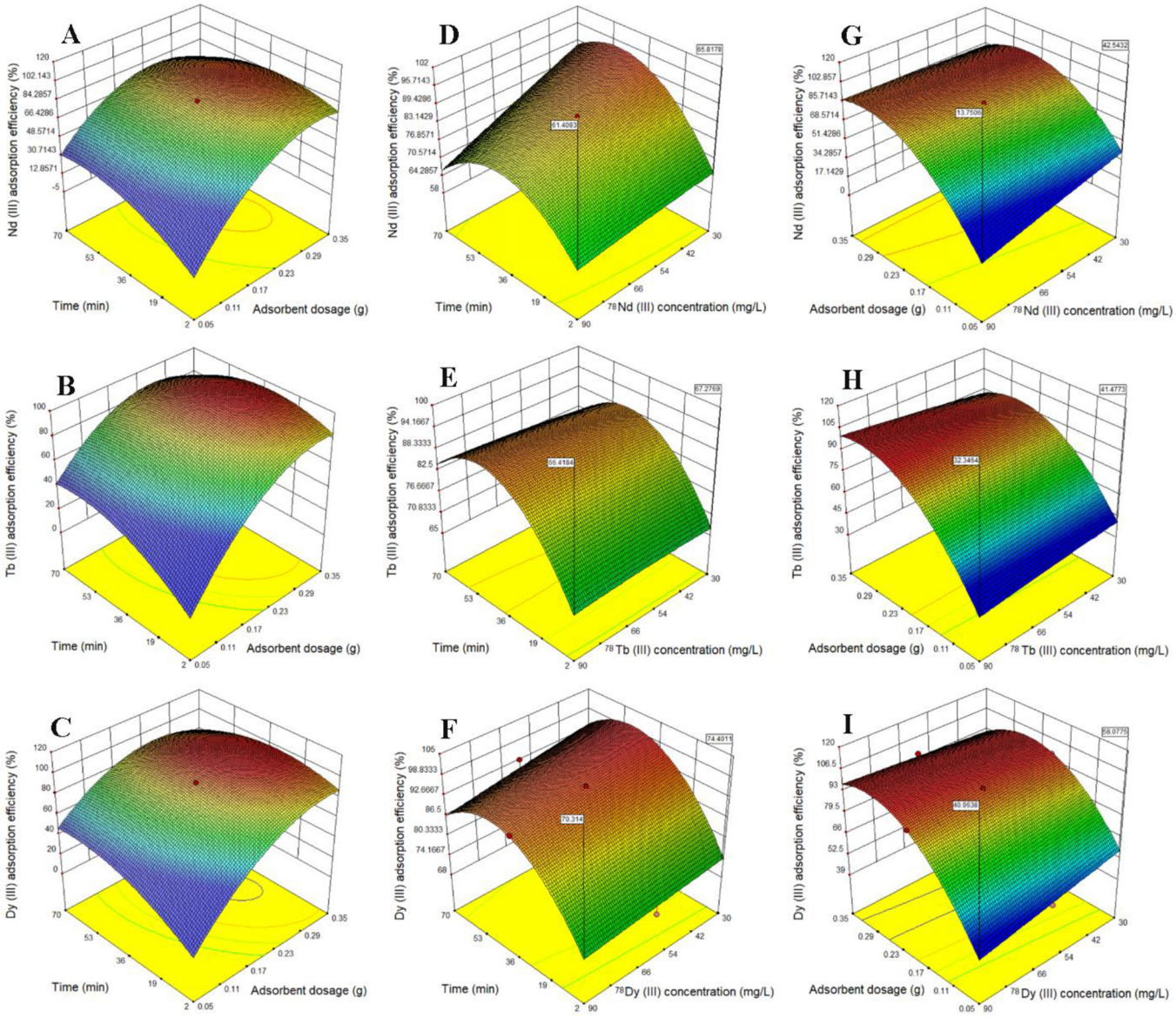
A
Nd (III) adsorption efficiency (%)
120
102.143
84.2857
66.4286
48.5714
30.7143
12.8571
-5
Time (min)
70
53
36
19
2
Adsorbent dosage (g)
0.05
0.11
0.17
0.23
0.29
0.35
D
Nd (III) adsorption efficiency (%)
102
95.7143
89.4286
83.1429
76.8571
70.5714
64.2857
58
85.8178
81.4093
Time (min)
Nd (III) concentration (mg/L)
90
66
54
42
30
G
Nd (III) adsorption efficiency (%)
120
102.857
85.7143
68.5714
51.4286
34.2857
17.1429
0
42.5432
13.7506
Adsorbent dosage (g)
Nd (III) concentration (mg/L)
B
Tb (III) adsorption efficiency (%)
100
80
60
40
20
0
Time (min)
Adsorbent dosage (g)
E
Tb (III) adsorption efficiency (%)
100
94.1667
88.3333
82.5
76.6667
70.8333
65
87.2769
85.4184
Time (min)
Tb (III) concentration (mg/L)
H
Tb (III) adsorption efficiency (%)
120
105
90
75
60
45
30
41.4773
32.2484
Adsorbent dosage (g)
Tb (III) concentration (mg/L)
C
Dy (III) adsorption efficiency (%)
120
100
80
60
40
20
0
Time (min)
Adsorbent dosage (g)
F
Dy (III) adsorption efficiency (%)
105
98.8333
92.6667
86.5
80.3333
74.1667
68
74.4911
70.314
Time (min)
Dy (III) concentration (mg/L)
I
Dy (III) adsorption efficiency (%)
120
106.5
93
79.5
66
52.5
39
68.9775
60.9638
Adsorbent dosage (g)
Dy (III) concentration (mg/L)

Figure 12

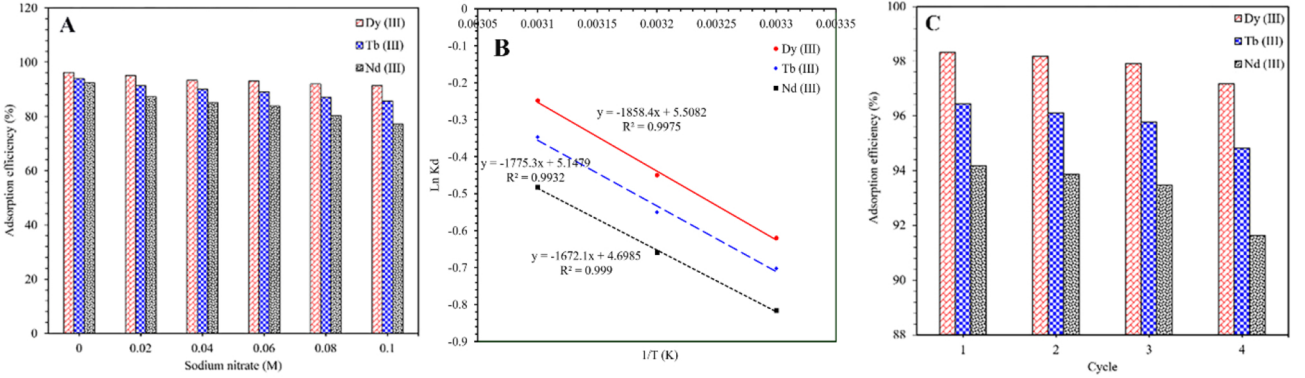
A
Dy (III)
Tb (III)
Nd (III)
Adsorption efficiency (%)
Sodium nitrate (M)
0
0.02
0.04
0.06
0.08
0.1
B
Ln Kd
1/T (K)
y = -1858.4x + 5.5082
R² = 0.9975
y = -1775.3x + 5.1479
R² = 0.9932
y = -1672.1x + 4.6985
R² = 0.999
C
Adsorption efficiency (%)
Cycle

Figure 13

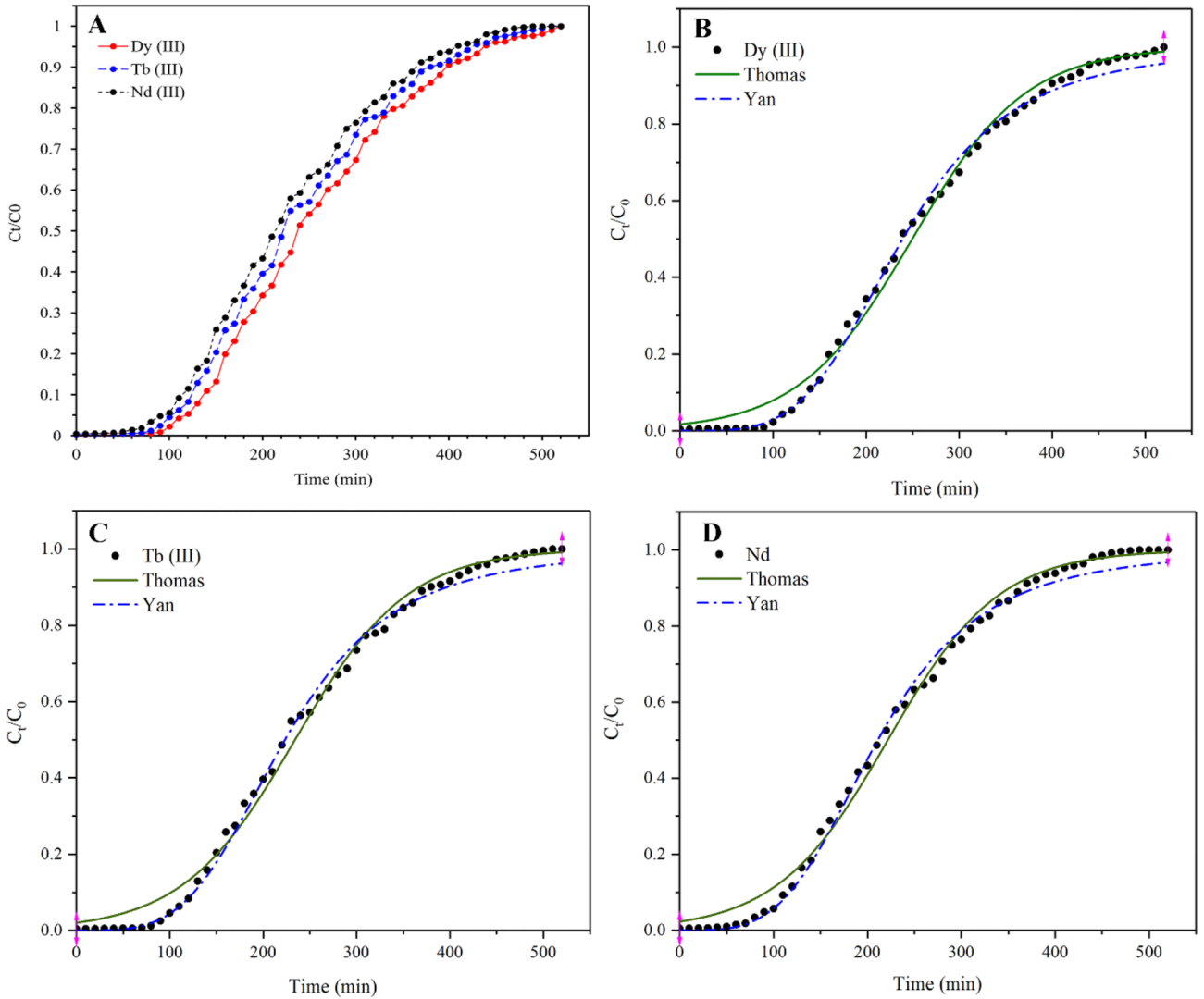
A
Dy (III)
Tb (III)
Nd (III)
Ct/C0
Time (min)
B
Dy (III)
Thomas
Yan
Ct/C0
Time (min)
C
Tb (III)
Thomas
Yan
Ct/C0
Time (min)
D
Nd
Thomas
Yan
Ct/C0
Time (min)

Figure 14